UC Santa Barbara

UC Santa Barbara Previously Published Works

Title

The combined influence of ENSO and PDO on the spring UTLS ozone variability in South America

Permalink

https://escholarship.org/uc/item/8b42k0jt

Journal

Climate Dynamics, 55(5-6)

ISSN

0930-7575

Authors

Gamelin, Brandi L
Carvalho, Leila MV
Kayano, Mary

Publication Date

2020-09-01

DOI

10.1007/s00382-020-05340-0

Peer reviewed

Evaluating the influence of deep convection on tropopause thermodynamics and lower stratospheric water vapor: A RELAMPAGO case study using the WRF model

Brandi L. Gamelin [a,*], Leila M.V. Carvalho [a,b], Charles Jones [a,b]

[a] *Department of Geography, University of California, Santa Barbara, United States of America*
[b] *Earth Research Institute, University of California, Santa Barbara, United States of America*

A B S T R A C T

Troposphere to stratosphere exchange is generally driven by deep convection capable of overshooting tropospheric materials contributing to stratospheric chemistry. The La Plata Basin region in South America is known for organized deep convection and mesoscale convective systems. This study employs the Weather Research and Forecasting model to simulate deep convection during the RELAMPAGO field campaign in Argentina. This work investigates upper troposphere – lower stratosphere (UTLS) thermodynamics, specifically double tropopause events, and identifies lower stratospheric hydration related to deep convection. Results show that lower stratospheric hydration occurred during two organized convective types, a mesoscale convective complex (MCC) and squall line, which coincided with strong low level jet moisture transport. However, the lower stratosphere was not hydrated during discrete cells. While UTLS moisture was present in all three convective types, during the discrete cell, ice and water vapor were mixed, inhibiting net positive buoyancy and the transport of tropospheric material aloft. During the MCC and squall line events, UTLS moisture was stratified. A dry layer in the tropopause was collocated with an ice layer where net positive buoyancy contributed to stratospheric hydration as high as 20 km.

1. Introduction

The tropopause region is known for troposphere-stratosphere exchanges, and in the lower stratosphere the presence of water vapor is known to influence Earth's radiation budget (Holton et al., 1995). Because air primarily enters the stratosphere in the tropics, the air near the tropical tropopause behaves as a boundary for the global stratosphere (e.g. Brewer, 1949). In this regard, most changes to the lower stratosphere are generally attributed to the vertical transport of tropospheric gases during deep convection at the tropical tropopause boundary (Khaykin et al., 2009). Outside the tropics, the influence of deep convection on tropopause thermodynamics and lower stratosphere hydration is less understood. Additionally, in the extratropics, moist deep convection can alter UTLS thermodynamics, contribute to atmospheric folding (e.g. double tropopause) and ultimately influence the detrainment of ice and water vapor in the lower stratosphere.

Globally speaking, UTLS double tropopause features generally occur where the height of the tropopause decreases rapidly between the subtropics and sub-polar regions (Pan et al., 2004; Homeyer et al., 2014a). In South America, this is observed in the southern La Plata Basin (LPB), where double tropopause events tend to be collocated to the upper-level jet stream and may occur over the central Andes throughout the year (Peevey et al., 2012). The presence of a double tropopauses may influence the height of maximum water vapor levels in the stratosphere (Homeyer et al., 2014a) and ultimately ozone chemistry.

Changes to stratospheric chemistry are reliant on the transport of tropospheric gasses to the stratosphere, especially water vapor. Water vapor in the stratosphere chemically reacts to become a catalyst for stratospheric ozone destruction (Bates and Nicolet, 1950). In the stratosphere, ozone (O_3) chemically responds to incoming ultraviolet (UV) radiation to produce excited oxygen atoms ($O(^1D)$). When $O(^1D)$ atoms interact with water vapor (H_2O), the response produces the hydroxyl free radical (($O(1D) + H_2O \rightarrow 2OH$)) (e.g. Seinfeld and Pandis, 1998). Furthermore, when OH interacts with O_3 it is converted to two oxygen molecules ($O_3 + OH \rightarrow 2O_2$). Ultimately, O_3 in the stratosphere absorbs harmful UV radiation and water vapor becomes a catalyst for

---

OH production and O_3 destruction (Stenke and Grewe, 2005), resulting in increased UV radiation transferred to the troposphere (Forster and Shine, 2002).

Regions with deep convection capable of transporting water vapor to the stratosphere are generally understood to be localized in the tropics (Randel and Jensen, 2013; Hemanth et al., 2018; Ratnam et al., 2016). However, several studies have analyzed regions with convective overshooting in the subtropics and mid-latitudes (Laing and Fritsch, 1997; Brooks et al., 2003; Zipser et al., 2006; Bigelbach et al., 2014; Liu and Liu, 2016; Smith et al., 2017; Phoenix and Homeyer, 2021). Zipser et al. (2006) examined extreme thunderstorm events using several proxies for convective intensity and identified several regions with deep convection outside the tropics, including the central U.S. and southeast South America. They found cases in the United States, especially in the Midwestern region, where convective cloud top heights were capable of reaching up to 18.25 km.

Hurst et al. (2011) investigated water vapor in the lower stratosphere due to convective overshooting over Boulder, Colorado. They showed an increase in stratospheric water vapor of ~1 ppmv (almost 30%) between 16 and 26 km (~100–10 hPa) and found that modeled stratospheric water vapor trends are predominantly driven by two processes: the warming of the cold point temperature (CPT) and the strengthening of the Brewer-Dobson circulation. Tropopause boundary processes connected to CPT are the strongest regulator of cross boundary transport of gasses to and from the stratosphere.

Homeyer et al. (2014a) utilized the Weather Research and Forecasting (WRF) model to investigate the direct injection of water vapor in the stratosphere via deep convective processes in the central U.S. Their simulations reproduced the vertical extent of each convective system modeled and showed that double tropopause events were associated with tropospheric air higher in the stratosphere, compared to single tropopause events. Additionally, Homeyer et al. (2014b) investigated a Mesoscale Convective System (MCS) and a cold front with in-situ aircraft observations in the central United States. They found that large-scale double tropopause events may impact the level of water vapor mixing ratios deep into the lower stratosphere due to decreased UTLS stability.

While considerable research has been centered on the central United States, similarities exist between atmospheric dynamics, topography, and climatological features of the mid-west region of the United States and the LPB of South America. Both regions have a long north-south mountain range (Rocky Mountains in the U.S and Andes Mountains in South America), they are influenced by low-level jets transporting moisture from the tropics on the eastern side of the mountain chain (Higgins et al., 1997; Montini et al., 2019), and they have summer monsoonal processes that act to create conditions for the initiation and development of deep convective thunderstorm activity (Vera et al., 2006; Salio et al., 2007). Moreover, previous studies have shown that extratropical deep convection can hydrate the lower stratosphere via the detrainment of water vapor and ice crystals (Wang, 2003; Dessler and Sherwood, 2004; Le and Gallus, 2012; Homeyer et al., 2017; Smith et al., 2017). These processes have not been investigated over South America.

The LPB region in South America, including the Sierra De Cordoba and portions of the eastern Central Andes, is subject to deep convection and mesoracale convective systems (MCS; Rasmussen and Houze, 2016; Romatschke and Houze, 2010; Rasmussen and Houze Jr., 2011) capable of influencing the UTLS. The RELAMPAGO (Remote sensing of Electrification, Lighting and Mesoscale/microscale processes with adaptive Ground Observations) field campaign (November 1–December 16, 2018) was conducted to investigate convective processes in the LPB between Cordoba and San Rafael in Argentina (Nesbitt et al., 2021). The focus of this campaign was on initiation and intensity of convective systems in the region, especially the formation of severe weather. Although considerable research has been conducted to identify deep convection in the LPB, the influence of deep convection on the tropopause layer, exchanges between the troposphere and stratosphere, and the relationships between convection and double tropopause events

have not been investigated yet.

A major limitation of UTLS investigation in this region is the lack of high resolution spatial and temporal data capable of detecting UTLS exchanges. For instance, radiosonde launch sites in South America are sparsely located and generally not launched during severe thunderstorms. While radiosonde data in the LPB region can represent double tropopause features, they are less capable of identifying the maximum level of water vapor in the lower stratosphere and stratosphere – troposphere exchanges. Consequently, non-hydrostatic numerical models such as WRF (Skamarock et al., 2008) have been utilized to examine processes related to tropopause exchanges and overshooting (Robinson and Sherwood, 2005; Homeyer et al., 2014a; Homeyer, 2015). The primary goal of this work is to investigate mesoscale characteristics of deep convection in the LPB, identify double tropopause events and lower stratospheric hydration, and mechanisms related to large water vapor concentrations in the lower stratosphere with the WRF model.

In this study, mesoscale convective systems that occurred over a four-day period during the RELAMPAGO field campaign are simulated to answer the following questions, 1) have deep convective events hydrated the lower stratosphere in the LPB? If yes, can WRF simulate these events? 2) Are double tropopause events related to stratospheric hydration in the LPB? Lastly, 3) what are the primary mechanisms driving lower stratospheric hydration during double tropopause events in the LPB? These questions are addressed by simulating three types of deep convection: discrete convective cells, a mesoscale convective complex, and a squall line related to a cold frontal boundary. The study is organized as follows. The data is described in Section 2. The synoptic conditions related to the large-scale formation of deep convective events during this case study are described in Section 3. The WRF model configurations, sensitivity tests and model validations are described in Section 4. Stratospheric water vapor is discussed in Section 5. UTLS thermodynamics and lower stratospheric hydration is discussed in Section 6. Mechanisms explaining maximum water vapor between 15 and 20 km are described in Section 6.2. Conclusions are discussed in Section 7.

2. Data and methods

2.1. In-situ observations

Raw radiosonde data from November 10–15, 2018 for 00 and 12 UTC were obtained from the University of Wyoming Department of Atmospheric Sciences Weather online data archive (http://weather.uwyo.edu/upperair/sounding.html) for 8 stations in the greater La Plata Basin region in South America (see Section 3.2b).

2.2. Satellite data

The National Oceanic and Atmospheric Administration (NOAA) Geostationary Operational Environmental Satellite (GOES) Channel 13 infrared imagery, with a central wavelength of 10.3 μm, was employed to validate WRF simulated Outgoing Longwave Radiation (OLR). These images focused on the RELAMPAGO field campaign and are available from the National Center of Atmospheric Research (NCAR) and Earth Observing Laboratory (EOL) in Boulder, Colorado.

The National Aeronautics and Space Administration (NASA) Microwave Limb Sounder (MLS) is an instrument on NASA's Aura satellite and has supplied near-global, twice daily UTLS water vapor measurements since August 2004 (Lambert et al., 2020). The vertical range is from 316 hPa to 0.1 hPa, and the horizontal resolution is 210 km perpendicular and 7 km along Aura's orbital track (Read et al., 2007). MLS v2.2 H_2O data from November 10–14, 2018 was utilized to validate model water vapor mixing ratios at 5 pressure levels in the UTLS: 146.78, 121.15, 100, 82.54, 68.13, 56.23.

2.3. Reanalysis

The ERA-Interim reanalysis (ERAi) dataset produced by the European Centre for Medium-Range Weather Forecasts (ECMWF) (Simmons et al., 2006; Dee et al., 2011) was utilized to investigate synoptic-scale atmospheric conditions, and as initial and boundary conditions for the WRF model. ERAi horizontal resolution is approximately 0.75° latitude × 0.75° longitude (∼ 83 km) with 37 vertical levels from the surface to 0.1 hPa, available at 6-h intervals. The period of analysis extends from 00 UTC November 09 to 00 UTC November 15, 2018.

2.4. WRF model set up

WRF version 3.9.1.1 (Skamarock et al., 2008) was utilized to simulate the MCS in the La Plata Basin. Parameterizations employed in these simulations are shown in Table 1. Ruiz et al. (2010) performed WRF sensitivity testing of several model parameterizations in South America to identify optimal surface variables during the summer of 2003. They found that the best performing parameterizations included: the Yonsei University Scheme (YSU) for the Planetary Boundary layer physics (Hong et al., 2006) and the Unified Noah Land Surface Model for the Surface layer physics (Niu et al., 2011). Other cumulus parameterization schemes were tested with a coarser horizontal resolution (15 km, not shown), including the Kain–Fritsch (Kain, 2004), Grell–Freitas Ensemble (Grell and Freitas, 2014), Grell 3D Ensemble (Grell and Devenyi, 2002), Betts–Miller–Janjic (Janjic, 1994), and Tiedtke (Tiedtke, 1989; Zhang et al., 2011). The Grell-Freitas Ensemble scheme adequately simulated the size and location of the MCSs. Although additional experiments with WRF parameterizations are desirable, given our interest in reducing temperature uncertainties in the UTLS and identifying double tropopause features, this study focused on investigating the impacts of increasing vertical resolution by concentrating levels in the UTLS and in the boundary layer. Other parameterizations were held constant in this study and are listed in Table 1. The model set up for sensitivity testing of vertical resolutions is described in Section 4.

3. Synoptic description of events

GEOS 16 IR brightness temperature 6-h images (November 10 – November 15) illustrate the locations and progression of deep convection during the period of study (Fig. 1). Although deep convection occurred daily during this period, on November 12–13, 2018 a large, organized Mesoscale Convective Complex (MCC), located in northern Argentina, was of particular interest due to its strength and duration (Fig. 1). Additionally, this study investigates other convective systems that exhibited potential for strong updrafts and UTLS hydration. Because the MCC was the most disruptive event it will be considered the date of reference (Day 0) for the synoptic description of events.

Here, the large-scale atmospheric conditions are described from November 9–15 to show synoptic forcing from a pre-convection to post-convective environment (Figs. 2 and 3). Several general synoptic-scale features contributed to the formation of deep convection and MCS/ MCCs in the La Plata Basin. They include: (1) the position of the upper-level subtropical jet stream, which can perturb the atmosphere (Peevey

et al., 2012), and when combined with interactions with the Andes, can produce mountain/gravity waves that can result in double tropopause features (de laTorre et al., 2006); (2) the Bolivian High – an upper-level anticyclonic circulation typically positioned over Bolivia, (3) the Chaco Low – a surface level thermal low centered north the Sierra de Cordoba in Northern Argentina, and (4) the South American Low Level Jet (SALLJ) – a low level northerly wind jet that is often observed east of the Andes Mountain. The SALLJ is characterized by maximum wind speeds around 850 hPa and is responsible for heat and moisture transport from the tropics to the subtropics (Marengo et al., 2002, 2004; Montini et al., 2019). Previous studies have characterized extreme precipitation in Argentina related to the exit of the SALLJ (Salio et al., 2002, 2007). In the Southern LPB, as low-level moisture is transported across an active thermal low (e.g. the Chaco Low) and advected poleward, it approaches drier, cooler air at higher latitudes, and the resulting moisture flux convergence zone can contribute to convective initiation in this region (e.g. Rasmussen and Houze, 2016).

Lag-composites of 6-hourly mean sea level pressure and 850 hPa winds and upper-level winds (200 hPa) are shown in Figs. 2 and 3, respectively. Lags are relative to the date of the MCC on November 12 at 12 UTC (day 0; Fig. 1). On November 9 (day −3), a strong anticyclone was centered east of Southeast South America and was supported by upper-level convergence during a split upper-level jet event (Figs. 2 and 3, day −3). The position and strength of the anticyclone contributed to a low-level northerly flow and moisture transport from northern to central Argentina (Fig. 2, day −3). On November 10 (day −2), several discrete deep convective cells (DC) and clusters of cells were observed at approximately 32.5°S (Fig. 1, November 10). Deep convection with supercell structure and overshooting tops is shown in the GOES-16 visible image on November 10 at 15 UTC (Fig. 4; see Trapp, 2020 for details on this event). During this time, the anticyclone weakened and moved eastward, and a thermal low located near Cordoba, Argentina (Chaco Low) intensified as a trough crossed the Andes.

On November 11 (Fig. 2, day −1), the SALLJ strengthened, the Chaco Low was active, and the exit of the SALLJ was located in Argentina, west of Uruguay. These atmospheric conditions were consistent with the formation of organized convection in Southeast South America as discussed in Salio et al. (2007). The Salio et al. (2007) numerical experiment showed that one day before the development of an MCS, an active low level jet transporting heat and moisture to subtropical latitudes enhanced low level convergence near the exit of the SALLJ. Additionally, the same study showed that upper-level divergence corresponding to the position of a jet streak contributed to the development of a "long-lived" MCS. Similar conditions occurred on day −1 of this study and appear to have contributed to the intensification of organized deep convection.

On November 12 (Fig. 2, day 0), synoptic conditions were characterized by an active SALLJ and Chaco Low in the La Plata Basin, accompanied by a trough west of the Andes. In upper levels, east of Uruguay, divergence from a left entrance jet streak likely supported surface convergence and deep convection (Fig. 3, day 0). A large MCC was centered west of Uruguay. This MCC was also associated with the tornado that was reported by news outlets and social media near Reconquista and Goya in Northeastern Argentina. The MCC slowly propagated out of the area, prolonging the influence of deep convection until 18 UTC on November 13 (day +1). On day +1, a transient surface low pressure system (polar trough) associated with a cold frontal boundary positioned in Northern Argentina (approximately between 22 and 35°S), which can be identified by the convergence of winds and pressure gradients (Fig. 2). This location was similar to the position of the MCC on the previous two days, indicating sustained deep convection in the region. An organized band with deep convection (or squall line; SL) formed along the leading edge of the cold frontal boundary (Fig. 1, November 13), and is also investigated in this study. On November 14 (day +2), the low propagated equatorward and the frontal boundary migrated north into Paraguay and Brazil. As the system exited the

Table 1
Model parameters held constant for each simulation.

| Parameterizations for WRF model version v3.9.1. simulations (Skamarock et al., 2008)	
Cumulus	Grell–Freitas Ensemble (Grell and Freitas, 2014)
Boundary layer	Yonsei University (Hong et al., 2006)
Land surface	MM5 (Paulson, 1970)
Longwave radiation	RRTMG (Iacono et al., 2008)
Microphysics	Morrison 2–moment (Morrison et al., 2009)
Shortwave radiation	RRTMG (Iacono et al., 2008)
Surface layer	Noah-MP (Niu et al., 2011)
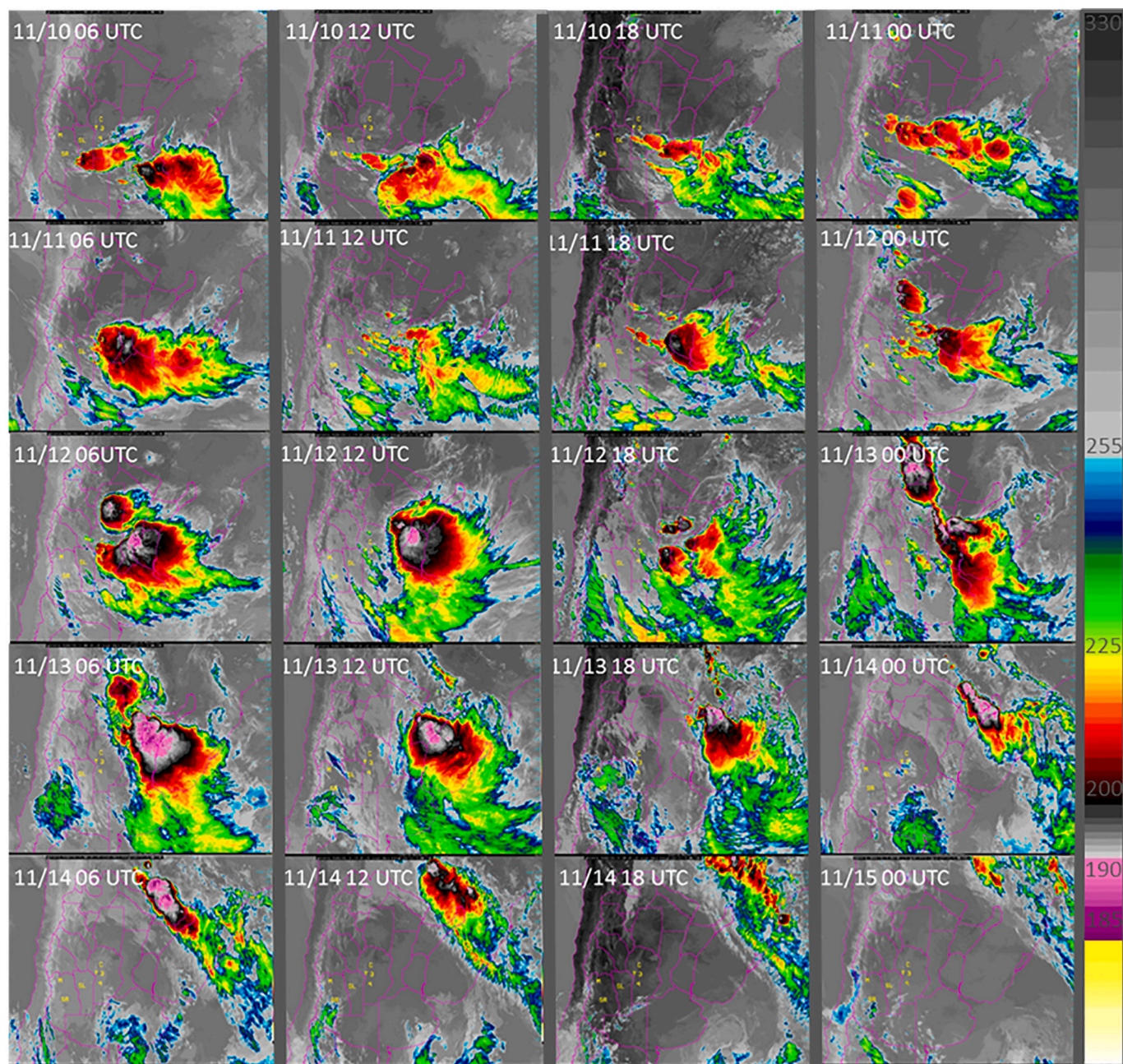
Fig. 1. GOES 16 channel 13 IR brightness temperature (K) every 6 h, November 10 06 UTC to November 15 00 UTC. Specific locations (yellow labels) on the IR images are related to the RELAMPAGO field campaign, including C: Cordoba, SL: San Luis, Y: Villa Yacanto, 3: Rio Tercero, 4: Rio Cuarto. (For interpretation of the references to colour in this figure legend, the reader is referred to the web version of this article.)

Southern La Plata Basin, a strong southerly flow associated with the position of the surface low contributed to stable, cool and dry conditions in the region.

4. WRF sensitivity experiment and validation

4.1. Testing vertical grid resolutions

The influence of deep convection on UTLS thermodynamics and exchange of water vapor was examined with WRF model simulations. These exchanges are strongly dependent on the profile of temperature and stability near tropopause level. Thus, sensitivity tests were conducted to evaluate the importance of increasing the vertical resolution in the UTLS to simulate observed double tropopause features. These

features can create thermodynamic instability at the UTLS conducive to lower stratospheric hydration. Model simulations were initiated on November 09, 2018 at 00 UTC and run until November 15, 2018, 00 UTC. Domains for the WRF simulations are shown in Fig. 5. The location of D01 was chosen to capture synoptic conditions surrounding the LPB, including low pressure systems propagating from the south or west, upper-level westerlies across the Andes, and low-level jet activities east of the Andes transporting heat and moisture; D03 was chosen based on the location of the mature MCC and deepest cloud cover on 12 November 2018 12 UTC (Fig. 1). The model was initiated with three 2-way nested domains and the first 12 h were regarded as spin-up, and not utilized for analysis.

WRF assigns vertical model levels based on the Eta (η) vertical coordinate system. Because primary analyses occur in the UTLS, with an
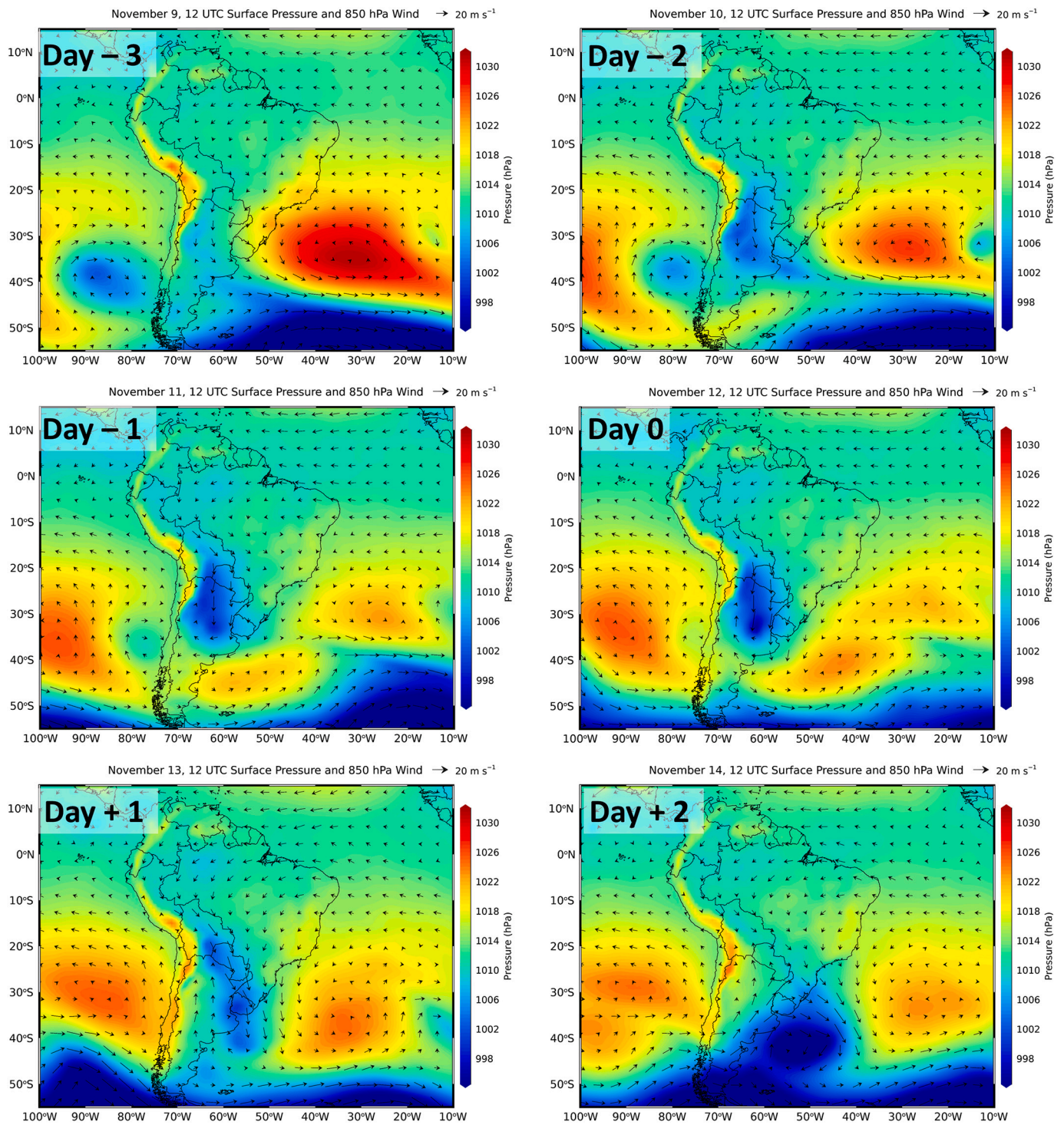
Fig. 2. ERAi mean sea level pressure (shaded) and 850 hPa wind (vectors) from 12 UTC November 9 – November 14, 2018. Each day is relative to the Mesoscale Convective Complex on 12 UTC November 12, 2018 (day 0) shown in Fig. 1.

emphasis on double tropopause events, vertical sensitivity testing was performed to identify the finest vertical resolution possible in the UTLS within the D03, 3 km horizontal grid spacing. Three model runs were conducted. First, WRF was initialized with 61,WRF assigned, η levels (R1; Fig. 5). WRF model levels for R1 are concentrated in the boundary layer to 2168 m, and then equally spaced (553.7 m) until the model top of 10 hPa (~29 km). The second WRF run (R2) was also initiated with 61 levels; however, the η levels were user assigned and concentrated in the boundary layer and tropopause region (R2; Fig. 5). To avoid abrupt

changes in height between eta levels and consequent instability errors, a third WRF run was proposed with 75 user assigned η levels. This configuration resulted in an optimum η levels that produced smoother height transitions. This simulation was an improvement over the first two runs as shown in the next section. All model parameterizations were held constant during each model run (Table 1). Radiosonde data were not assimilated in these simulations.
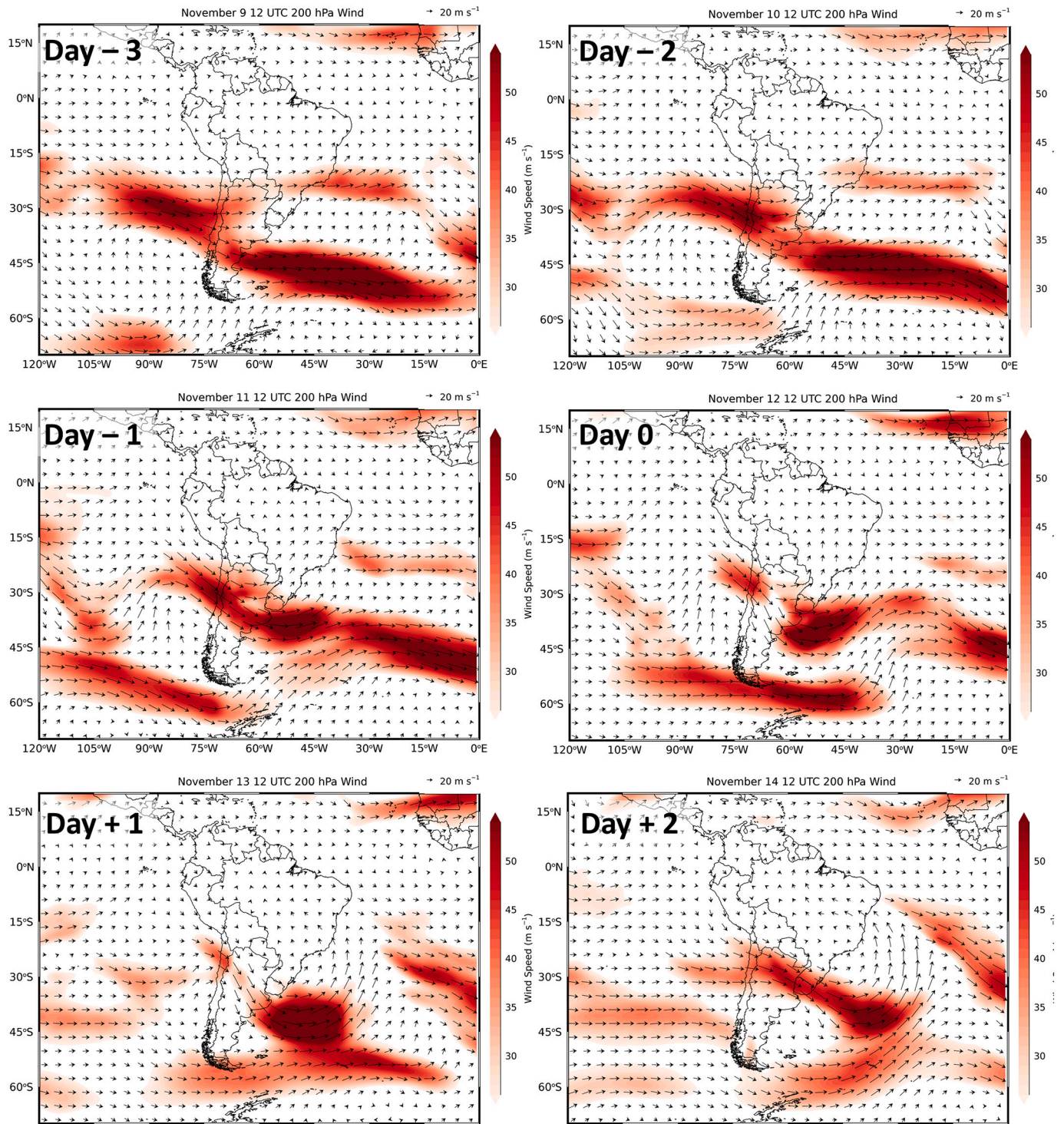
Fig. 3. ERAi 200 hPa wind (vectors) from November 12–14, 2018 at 12 UTC. Shading represents 200 hPa zonal winds (only zonal winds above 25 m s^{-1} are shaded).

4.2. Model validation

Model skill is initially evaluated with infrared (IR) satellite imagery. WRF simulated outgoing longwave radiation (OLR) is utilized as a proxy for cloud top temperature and height (Gutzler and Wood, 1990) and compared to satellite imagery (Fig. 6). Clustered discrete cells are shown on November 10, 2018 at 21 UTC and a Mesoscale Convective Complex on November 12, 12 UTC. Although the GOES 16 imagery and WRF domain are not the same, all three runs appear to adequately simulate

the extent of deep convection during both time frames, with a few structural differences distinguishing the three runs. While the importance of simulating deep convection cannot be overstated, the main goal for these simulations is to identify double tropopause features and lower stratospheric hydration during deep convection. Therefore, we validated these runs with soundings emphasizing available upper troposphere – lower stratosphere temperature and humidity data, and with MLS satellite water vapor data.

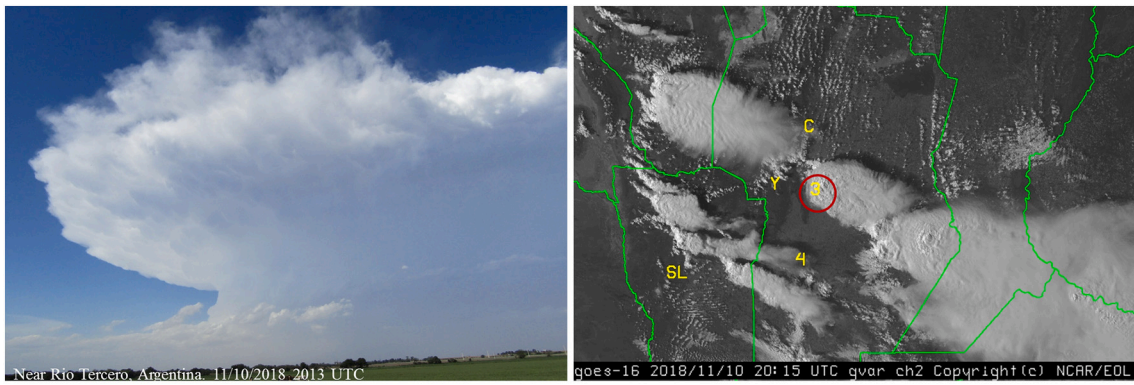Raw radiosonde data from November 10–15, 2018 (00 and 12 UTC)

Fig. 4. Convective cell near Rio Tercero (red circle on right image), Argentina on November 10, 2018, at 20:13 UTC (left; photo by Brandi Gamelin). Corresponding GOES 16 channel 2 visible imagery at 20:15 UTC (right). Specific locations on the visible image are related to the RELAMPAGO field campaign, including C: Cordoba, SL: San Luis, Y: Villa Yacanto, 3: Rio Tercero, 4: Rio Cuarto. (For interpretation of the references to colour in this figure legend, the reader is referred to the web version of this article.)
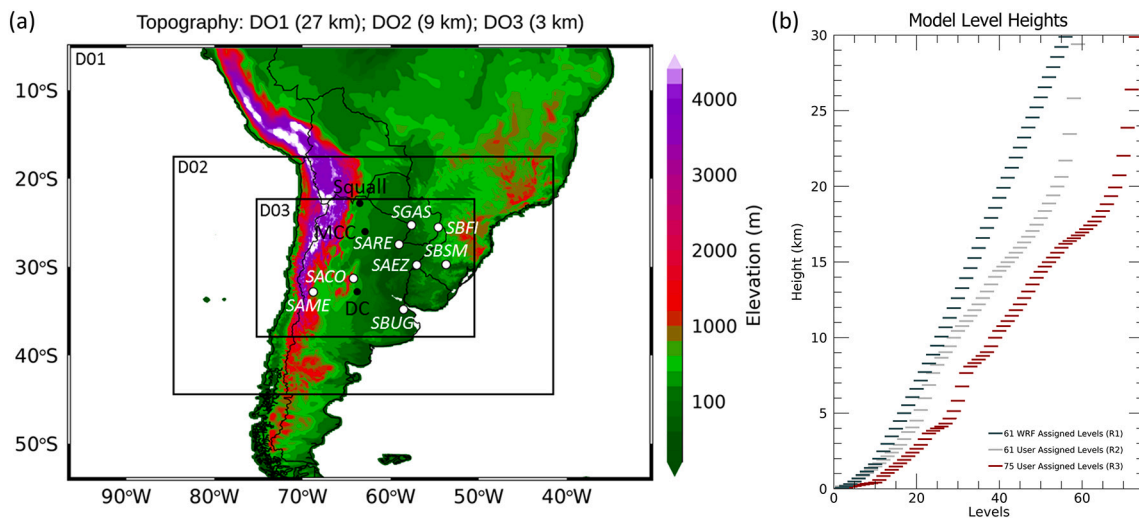

Fig. 5. (a) WRF model domains for downscaling to 3 km. Domains D01, D02 and D03 have 27 km 9 km and 3 km grid spacing resolution, respectively. Locations for radiosondes are represented with station ID (white italicized). Locations for detailed analysis in Section 6 are represented by black dots. (b) WRF vertical levels based on the Eta (η) vertical coordinate system for R1 (61 WRF assigned levels, dark grey), R2 (61 user assigned levels, light grey), and R3 (75 user assigned levels, red). See text for details. (For interpretation of the references to colour in this figure legend, the reader is referred to the web version of this article.)

from 8 stations in the greater La Plata Basin region in South America are discussed in Table 2 (see Section 2.1). Comparisons with WRF were performed at standard pressure levels from 925 to 70 hPa. Soundings without upper atmospheric data or soundings without standard pressure levels (e.g. SGAS) were omitted from model validation. Because of low water vapor mixing ratios and sharp gradients in the tropopause region, additional validation of UTLS water vapor was performed with MLS data from November 10–14, 2018 (locations are discussed in Table 2 - see Section 2.2).

Model root mean square error (RMSE) is utilized to assess simulated air temperature, relative humidity, wind speed and water vapor.

$$\text{RMSE} = \sqrt{\sum \frac{(pi - 0i)^2}{N}} \qquad (1)$$

RMSE is calculated for each model run and all available radiosonde data, where pi is model output and oi is radiosonde data. Stations with sounding data were chosen based on proximity to the MCC on November 12, 2018, and availability of data (Table 2). Observations were collected for 00 and 12 UTC and RMSE was calculated on standard pressure levels from 925 hPa to 70 hPa (Fig. 7). RMSE was also calculated with MLS water vapor data in the UTLS from 150 to 60 hPa.

Fig. 7 shows the vertical RMSE profiles using radiosonde temperature (1000–70 hPa), relative humidity (1000–100 hPa), and wind speed (1000–70 hPa), as well as MLS water vapor in the UTLS (150–60 hPa). Overall, the RMSE with radiosonde data is reduced in the R3 run compared to the R1 and R2 runs, especially for temperatures in the UTLS and the lower troposphere where model levels are concentrated. The RMSE with MLS is also reduced in R3 in the UTLS from 120 to 80 hPa, as compared to R2 and R1. The vertical mean RMSE for all three runs is summarized in Table 3.

RMSE was also calculated for air temperature at individual stations and for each WRF run separately (Fig. 8). Four locations with radiosonde data (SARE, SAME, SBSM, and SBFI; Table 2) were chosen based on locations relative to deep convection and available data.

The average temperature bias was calculated for each model run on standard pressure levels. Table 4 includes vertical mean temperature bias for each station location.

$$\text{Bias} = \frac{\Sigma(pi - oi)}{N} \qquad (2)$$

On average, for all stations, R1 bias is 1.54 K, R2 is 1.59 K, and R3 is 1.52 K. Overall, biases in temperature in R3 are reduced compared to R1 and R2, especially in the lower troposphere and UTLS where eta model
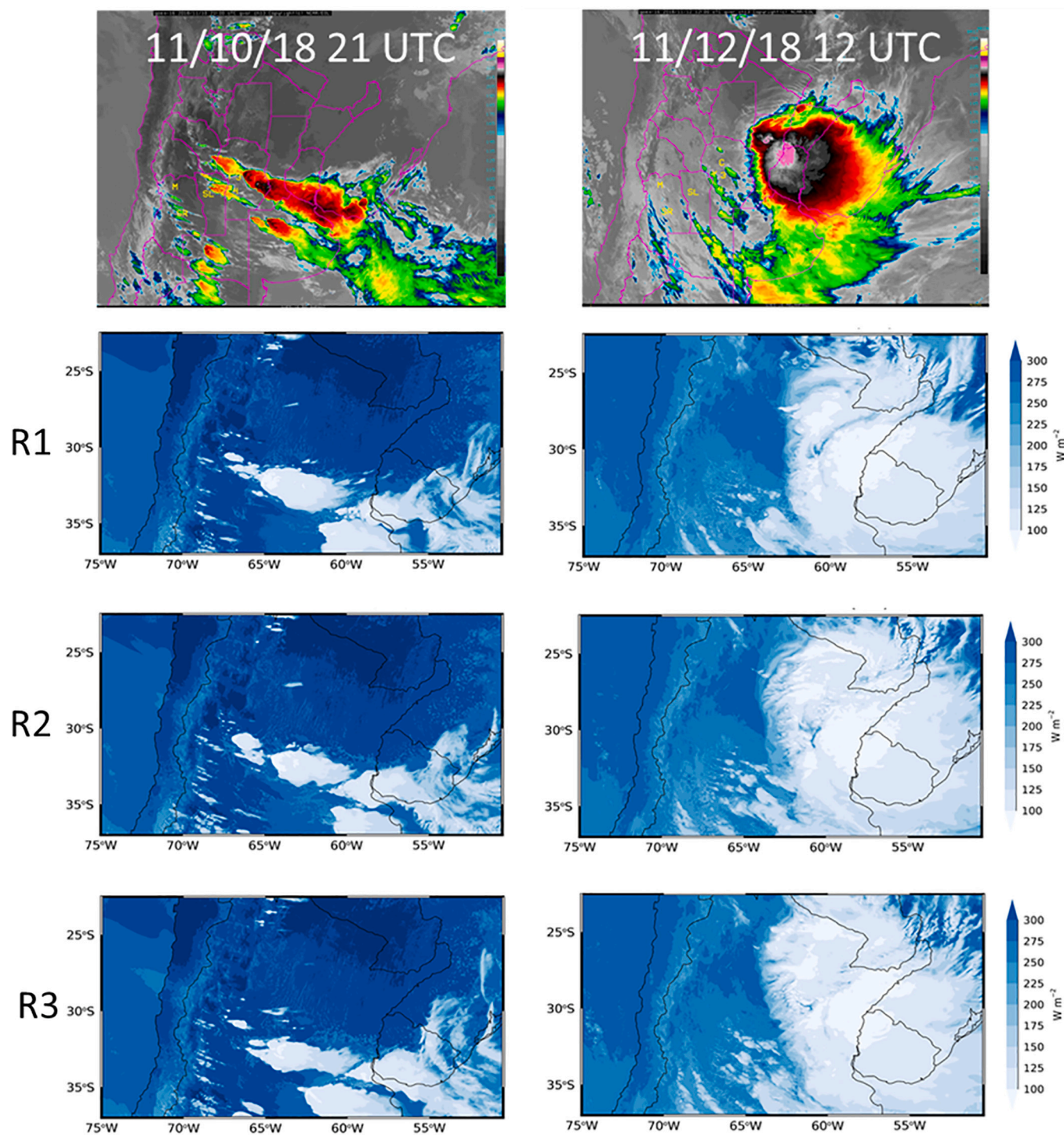
Fig. 6. WRF outgoing longwave radiation (OLR) for R1, R2 and R3, and GOES 16 clean infrared window 10.3 μm band 13 (image) on November 10, 2018 21 UTC (left) and November 12, 2018 12 UTC (right).

levels are concentrated.

Fig. 9 shows comparisons of simulated UTLS temperatures and radiosonde observations for three radiosonde sites: Santa Maria (SBSM), Foz do Iguacu Aero (SBFI) and Mendoza Aero (SAME). Two sites, the SBSM and SBFI, were directly impacted by the MCC, whereas SAME was representative of the environment where discrete and clustered cells were developed. The red lines are from radiosonde observations and show temperature features before the mature MCC on November 10, 2018 12 UTC (left column; Fig. 9) and post MCC November 15, 2018 00 UTC (right column; Fig. 9). Fig. 9 (center column) shows profiles during

the mature MCS phase for as near as the data is available. Overall, R3 (solid black line) with 75 user assigned model levels demonstrates best performance in reproducing UTLS temperature profiles compared to the observed temperatures. Of particular importance for this study is the profile between 90 and 60 hPa, where R3 seems to better reproduce the observed double tropopause.

Throughout the validation process, R3, which has user assigned WRF model levels concentrated in the boundary layer and UTLS, has been shown to minimize model error compared to R1 and R2. More importantly, R3 has been shown to simulate double tropopause features that

Table 2
Top: list of radiosonde stations: abbreviation (id), number, location, latitude, longitude and launch time. Bottom: list of MLS locations and dates.

Id.	Number	Location	Latitude	Longitude	Launch time (UTC)
Radiosonde data					
SACO	87,344	Cordoba Aero	−31.30	−64.21	00 and 12
SAEZ	87,576	Ezeiza Aero	−34.81	−58.53	12
SAME	87,418	Mendoza Aero	−32.83	−68.78	00 and 12
SARE	87,155	Resistencia Aero	−27.45	−59.05	00 and 12
SBFI	83,827	Foz Do Iguacu Aero	−25.51	−54.58	00 and 12
SBSM	83,937	Santa Maria	−29.72	−53.70	00 and 12
SBUG	83,928	Uruguaiana	−29.78	−57.03	00 and 12
SGAS	86,218	Asuncion	−25.26	−57.63	12

Date	Latitude	Longitude	Date	Latitude	Longitude
Microwave Limb Sounder Data					
	−28.1821	−62.7891	13th	−31.1407	−62.3935
	−29.6620	−63.1665		−28.1815	−63.1548
	−32.6200	−63.9517		−25.2203	−63.9177
10th	−32.6193	−54.2684		−23.7389	−64.2790
	−32.6193	−65.0855	14th	−23.7392	−55.5082
	−31.1407	−65.4814		−26.7016	−56.2393
11th	−29.6614	−65.8653		−31.1413	−57.3749
	−26.7016	−59.3273			
	−28.1821	−59.7016			
12th	−32.6199	−60.8643			

are not generally exhibited in R1 or R2. For the remainder of this study, R3 configuration is used for analysis.

5. Lower stratospheric water vapor

5.1. Convective types and lower stratospheric water vapor

This analysis focuses on the three categories of MCSs discussed in Section 4 (DC, MCC and SL; Mulholland et al., 2018). Fig. 10 shows each category based on outgoing longwave radiation (OLR) and the associated water vapor mixing ratios at 100, 90, 80, and 70 hPa. Water vapor mixing ratios above 4.0 ppmv are noted as mixing ratios above background levels in Dauhut et al. (2018). In our study, we assumed the same background water vapor mixing ratio in the lower stratosphere (4.0 ppmv) since the simulated levels were generally between 1 and 4 ppmv during times when convection was not deeply developed (not shown).

The three types of deep convection analyzed here are shown on three sequential days. The first type was a DC observed in the subtropics at approximately 32°S. This type was located in the southern La Plata Basin at 21 UTC on November 10, 2018. For the DC, notable water vapor concentrations above background levels are shown at 100 and 90 hPa (Fig. 10, column 1). The second type is the MCC observed in northern Argentina at 06 UTC on November 12, 2018. For the MCC, water vapor concentrations above background levels are primarily shown in subtropical locations from approximately 24–30°S and at altitudes as high as 70 hPa (Fig. 10 column 2). The third type is a SL with a NW-SE orientation, extending from the Andes Mountains in western Paraguay to eastern Uruguay and the Atlantic Ocean at 06 UTC on November 13, 2018. For this system, water vapor concentrations above background levels span from 22 to 35°S. The highest levels are located at approximately 22°S and at altitudes as high as 80 hPa (Fig. 10 column 3).

It is important to note that water vapor in the stratosphere above 40 hPa can be created via methane (CH_4) oxidation: $CH_4 + OH$ becomes $CH_3 + H_2O$ (Bates and Nicolet, 1950; Le Texier et al., 1988). As previously discussed, stratospheric water vapor chemically reacts to destroy ozone. In the mid and upper stratosphere, chemically converted methane is the primary source of water vapor (Brasseur and Solomon, 2005). Nonetheless, the WRF model utilized for this work does not include stratospheric water vapor chemistry. Therefore, the water vapor

concentrations in the lower stratosphere (Fig. 10) that were not related to the detrainment of water vapor through deep convection were likely due to water vapor advected from other locations or diabatic descent related to cooling and transport from above in the model. These mechanisms explaining water vapor transport in the WRF simulations are not discussed in this study.

5.2. Tropospheric flow and lower stratospheric water vapor

Mullendore et al. (2005) used a three-dimensional cloud-resolving model to analyze troposphere to stratosphere transport with idealized supercell and multicellular storms. They found that source regions in the lower troposphere contributed to irreversible transport to the stratosphere. As described in Section 3, the SALLJ is a significant source of heat and moisture in the study region (e.g. Marengo et al., 2002, 2004; Montini et al., 2019). This low-level transport is generally responsible for convergence (Vernekar et al., 2003), moisture flux (Berbery and Collini, 2000), and extreme precipitation related to the exit of the SALLJ (Salio et al., 2002, 2007). Although many factors may contribute to the lower stratosphere hydration, here we investigate the influence of moisture flux convergence and moisture transport in the lower troposphere during times of maximum water vapor concentrations in the lower stratosphere.

Fig. 11(a, b and c) shows maximum water vapor mixing ratios in the lower stratosphere between 15 and 20 km related to deep convection. These concentrations were obtained by finding grid points with WRF OLR values less than 100 W m^{-2}, which was used as a proxy for deep convection (e.g. Massie et al., 2002). These points indicate regions where tropopause dynamical processes may be relevant in UTLS water vapor concentrations. Additionally, moisture flux at 850 hPa (Fig. 11d, e and f), which is the level identified as the wind maxima related to the SALLJ (Marengo et al., 2004; Jones, 2019; Montini et al., 2019), was calculated to investigate the role of the meridional moisture transport by the SALLJ and investigate timeframes of enhanced water vapor in the UTLS. Moisture flux convergence (MFC; Fig. 11g, h and i) at 950 hPa was calculated based on Banacos and Schultz (2005). The MFC equation (Eq. (3)) combines two terms: the horizontal advection of water vapor and the product of water vapor and horizontal mass convergence.

$$\text{MFC} = \left[-u\frac{\partial q}{\partial x} - v\frac{\partial q}{\partial y} \right] + \left[-q\left(\frac{\partial u}{\partial x} + \frac{\partial v}{\partial y}\right) \right] \tag{3}$$

MFC is a useful measure of low-level moisture transport and convergence (e.g. Rasmussen and Houze Jr., 2011; Baisya and Pattnaik, 2019), and the Eq. (3) has been applied at 950 hPa to identify low level convergence (positive MFC) and divergence (negative MFC).

Moisture transport and low-level convergence is evident during each convective type (Fig. 11). For the MCC type, strong meridional moisture transport occurs at 850 hPa (Fig. 11e), and at 950 hPa, the converging outflow boundary nearly surrounds the system (Fig. 11 h, red line). For the SL type, strong meridional moisture transport is also shown at 850 hPa (Fig. 11f), and at 950 hPa, the gust front spans from 22 to 35°S (Fig. 11i, red line). Although the DC type of deep convection is associated with a convergent boundary at 950 hPa (Fig. 11g, red line), meridional wind and moisture transport in the lower troposphere are weaker when compared to the MCC and SL (Fig. 11d).

Additionally, during the MCC, a strong outflow boundary along the northern gust front (Fig. 11h) likely triggered new cell development and prolonged the MCC life cycle. During this time frame, the enhanced low level moisture transport and convergence is evident and may have contributed to enhanced maximum water vapor shown in the lower stratosphere. The MCC is investigated further in the next section.

5.3. Deep convection and water vapor in the UTLS

Here we begin to characterize mechanisms relating deep convection
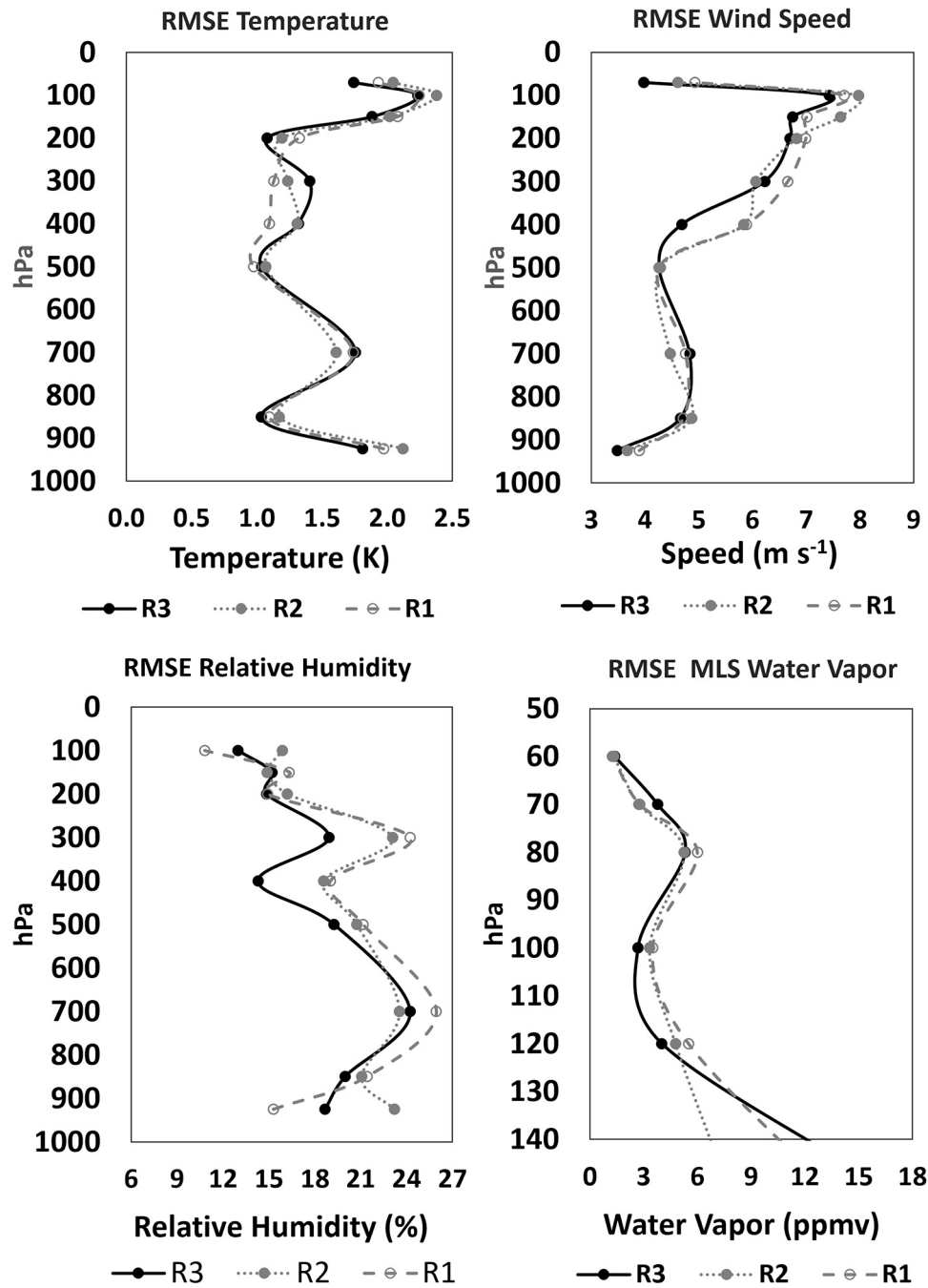
Fig. 7. Model root mean square error (RMSE) for temperature, wind speed and relative humidity using on radiosonde data, and RMSE for water vapor using MLS data. Note, RMSE of water vapor is for the UTLS region only.

Table 3
Vertical mean RMSE with radiosonde temperature, relative humidity, and wind speed, and with MLS water vapor.

	Vertically mean RMSE		
	R1	R2	R3
Temperature (K)	1.5587	1.6156	1.5306
Relative Humidity (%)	17.6013	18.4194	16.5775
Wind Speed (m s^{-1})	5.6796	5.6244	5.3007
Water Vapor (ppmv)	5.604008	4.1899	5.3746

and water vapor variability in the UTLS. OLR was used here to objectively identify contiguous convective regions associated with the MCSs, following a similar approach as in Carvalho and Jones (2001) and Ferreira et al. (2003). Contiguous cloud clusters with OLR less than 100 Wm^{-2} were examined to identify properties of the MCSs that appeared related to water vapor transport to the lower stratosphere. Among all convective types, the MCC has the largest maximum water vapor in the lower stratosphere. Furthermore, the MCC is related to the strongest dynamical forcing in the lower troposphere, identified by strong winds speeds, and the strongest updrafts and downdrafts at 100 hPa and 500 hPa, which likely contributed to maximum water vapor concentration in the lower stratosphere.
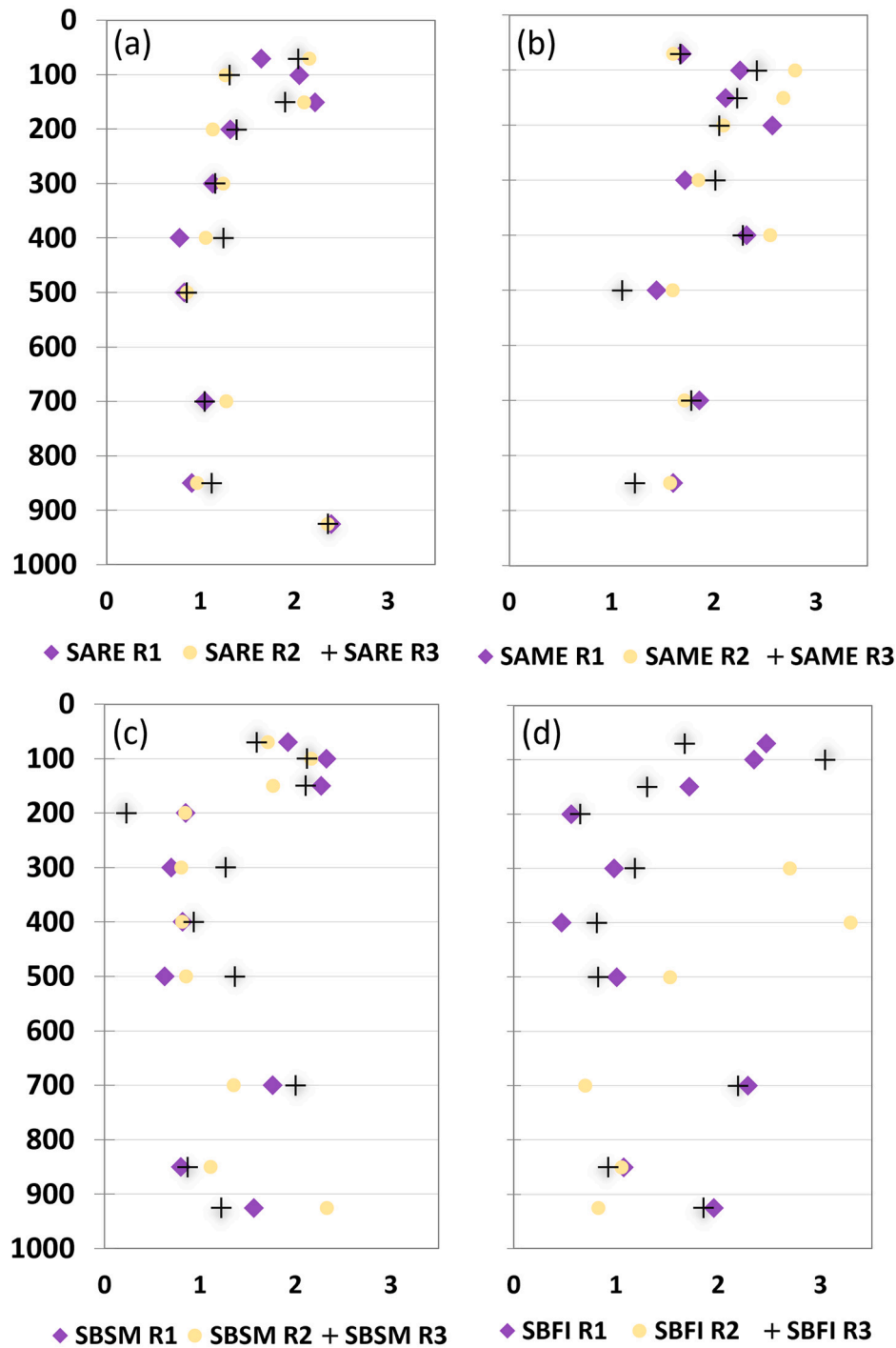
Fig. 8. Temperature (K) RMSE from SARE (a), SAME (b), SBSM (c), and SBFI (d).

Table 4
Vertical mean temperature (K) bias for the SARE, SAME, SBSM, and SBFI stations.

	Vertical mean temperature bias (K)		
	R1	R2	R3
SARE	1.44240	1.44098	1.44123
SAME	1.95068	2.04901	1.86440
SBSM	1.34069	1.26932	1.38715
SBFI	1.43439	1.57987	1.40128

To better understand these processes, we tracked clusters of deep convection focused on the MCC. Limitations due to cell duration and domain size prevented cell tracking for the DC (e.g. short lived discrete cell) and the Squall line (e.g. system propagates outside the domain). The MCC system has a prolonged influence within the domain allowing us to track a cluster of deep convection from pre-MCC to post-MCC. For this purpose, we tracked the long-lived MCC in 3-h intervals for 18 h between November 11, 21 UTC – November 12, 15 UTC. Fig. 12 illustrates the maximum water vapor in each grid point between 90 and 70 hPa for each tracked cluster.
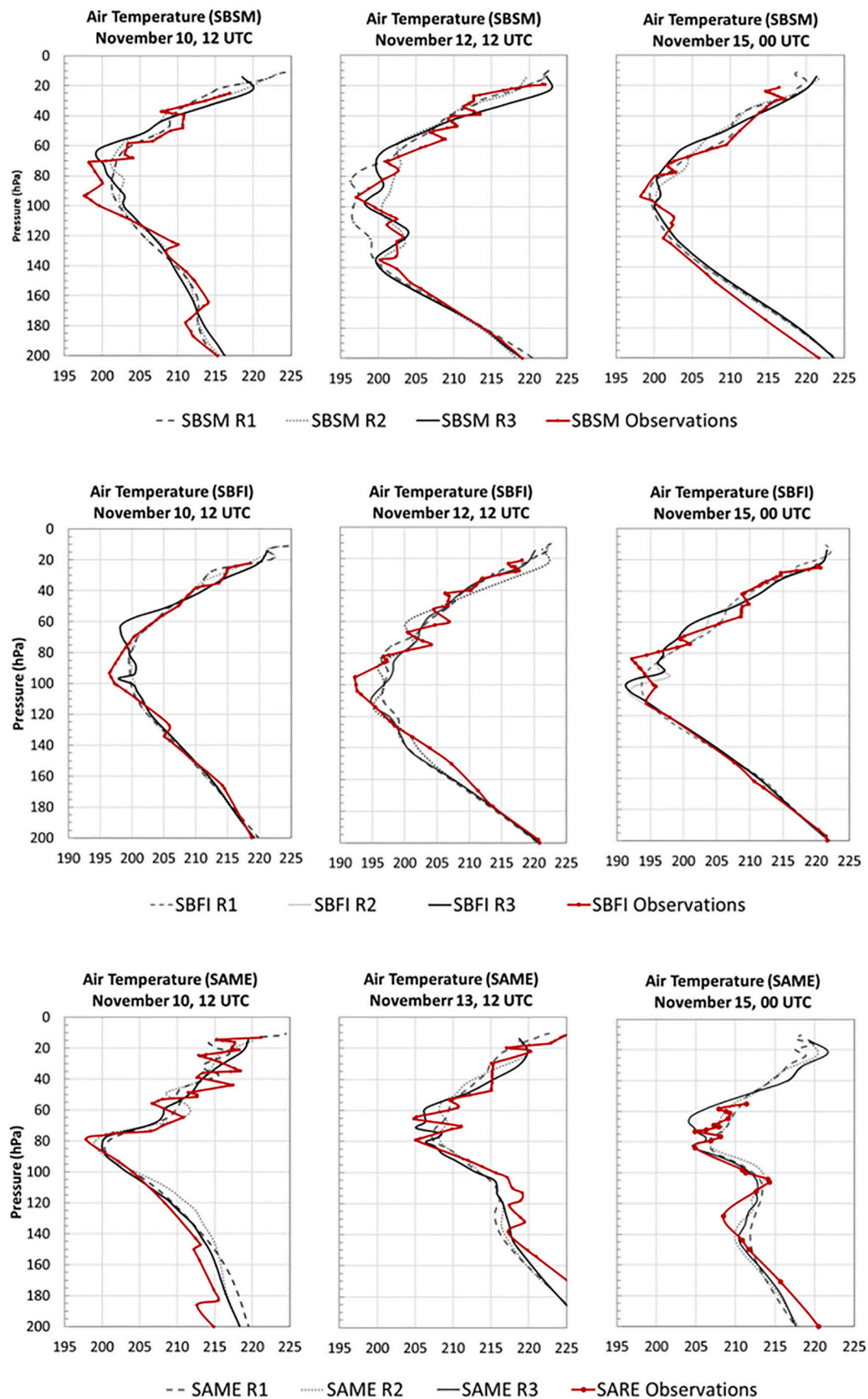
Fig. 9. Air temperature profiles for 3 stations: SBSM (top row), SBFI (middle row), and SAME (bottom row). UTLS WRF temperature for R1 (dashed line), R2 (dotted line) and R3 (solid line), and observations (red line). (For interpretation of the references to colour in this figure legend, the reader is referred to the web version of this article.)
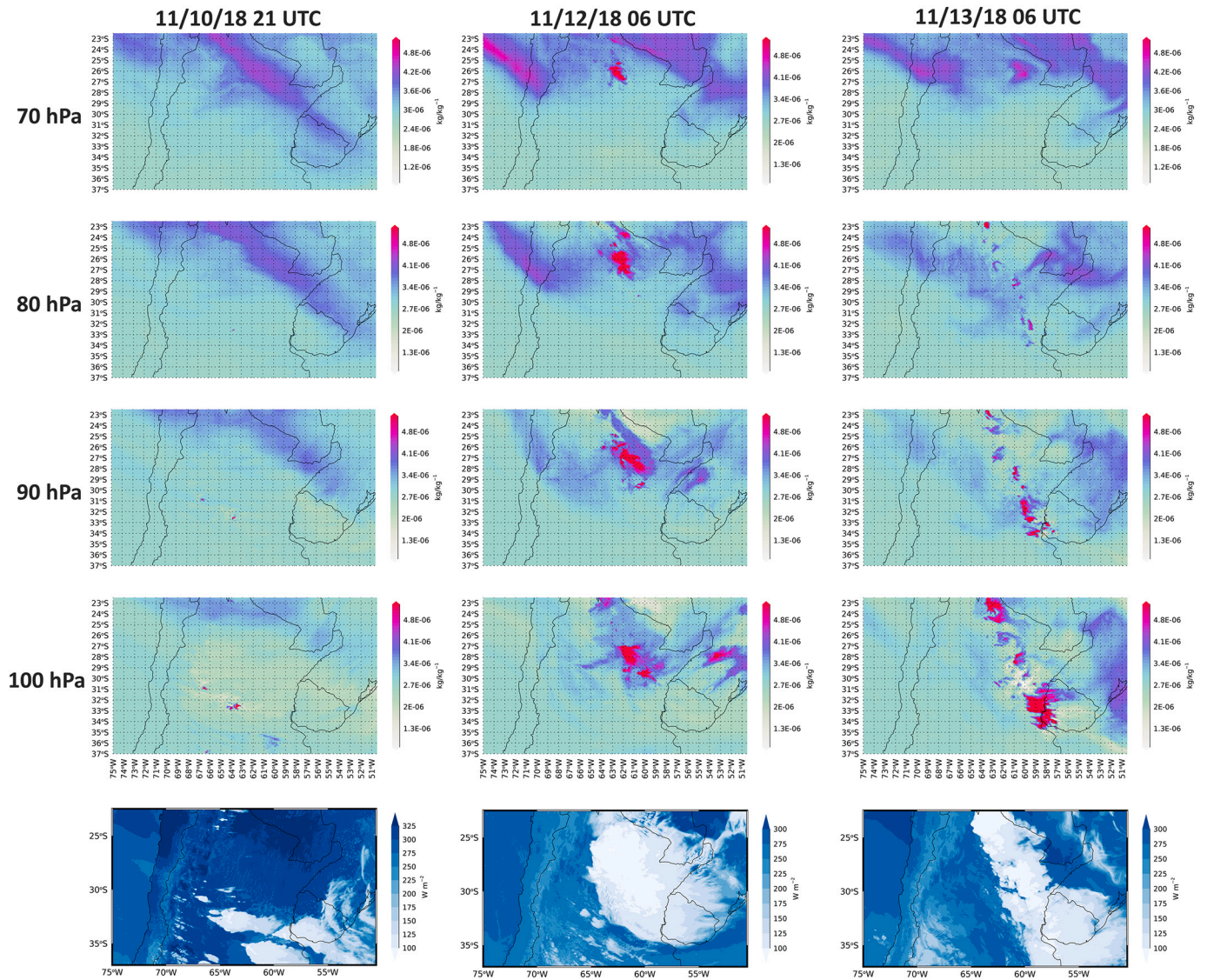
Fig. 10. WRF water vapor mixing ratio at 100, 90, 80, and 70 hPa for three convective types: November 10, 2018 21 UTC (left column), November 12, 2018 06 UTC (middle column), and November 13, 2018 06 UTC (right column); WRF outgoing longwave radiation for the same periods is shown in the bottom panel.

Seven hours during the evolution of the MCC are analyzed and results are summarized in Table 5. Statistics were obtained for the entire cloud cluster (defined by the OLR threshold of 100 Wm^{-2}) and for grid points that exceeded the threshold of 4.2 ppmv (assumed as background level) above 100 hPa. The following statistics are shown for each cloud cluster: total number of grid points in each cluster, area of these clusters (km^2), and maximum water vapor (ppmv). Additionally, grid points within these clusters exceeding the 4.2 ppmv threshold were examined and the following properties were calculated: total number of grid points above the threshold, number of these grid points associated with double tropopauses (DT) and respective fraction of these points (see Section 6 for DT description). The maximum updrafts and downdrafts for each cluster were also computed (Table 5). At 21 UTC simulations show the largest maximum water vapor in the lower stratosphere related to the MCC and the smallest area (26,676 km^2), indicating early stages of development. We also observe the strongest updrafts during this stage (28.63 and 26.08 m s^{-1} at 500 and 100 hPa, respectively) that likely played a role in transporting water vapor to the UTLS. From this time onward, the MCC cloud cluster increased in area until 9:00 UTC, when the MCC area reached its largest area ($\sim$3.8 x10^{3}km^2), likely related to maximum expansion of the anvil cloud shields. After this time, the MCC

began to dissipate. Nonetheless, after 21 UTC updrafts and downdrafts decreased in intensity at 100 hPa, indicating that the convective support for transport of water vapor to the lower-stratosphere progressively weakens. The maximum water vapor at 100 hPa and between 90 and 70 hPa seemed well correlated with the maximum updrafts (Fig. 13a). As the system matures, and until dissipation begins, the number of grid cells exceeding 4.2 ppmv increased, despite the decrease in maximum updrafts. Possible mechanisms explaining this increase are explored next.

Notice that the strong updrafts associated with the MCC are consistent with observations in Heymsfield et al. (2010) in South America. In that study, updrafts reached 30 ms^{-1}, with vertical velocity maxima observed above 12 km, including some observations above 15 km. Heymsfield et al. (2010) hypothesized that latent heat release in upper levels initiated intense vertical motion and could explain the updraft maxima and height of updraft maxima in their study in South America. Additionally, Zipser et al. (2006) identified the location of the MCC in South America as a region of extreme thunderstorms, similar to the southern plains in the U.S Southern Great Plains (Giangrande et al., 2013). We observe similar features in our simulations. Maximum updrafts of 28.63 ms^{-1} and 26.08 were observed at 100 hPa and 500 hPa at 21:00 UTC, respectively. Downdrafts at 100 hPa and 500 hPa were
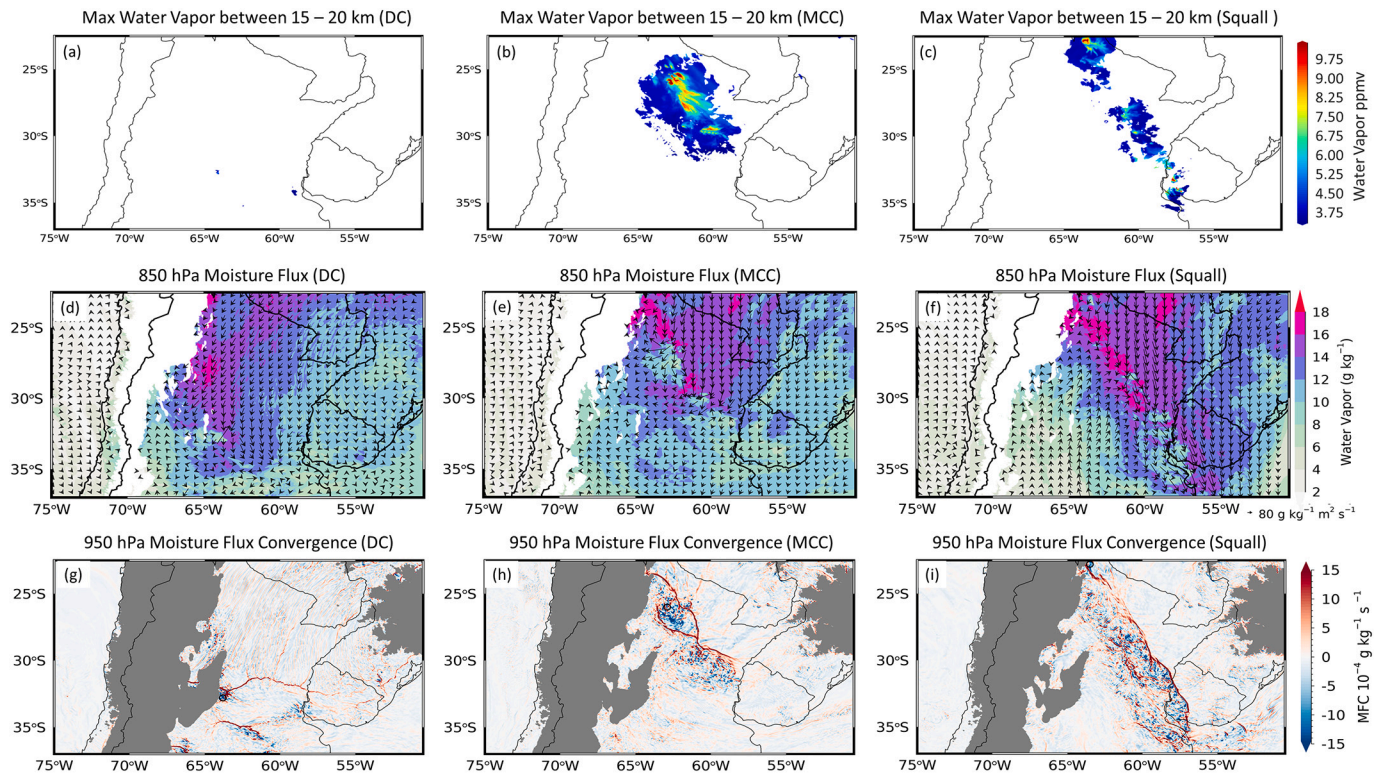
Fig. 11. Three types of convection: discrete deep convection (DC; a, d, and g), mesoscale convective complex (MCC; b, e and h) and squall line (Squall; c, f and i). Grey and white areas indicate terrain at the given pressure levels. Top row (a-c): maximum water vapor (15–20 km) related to deep convection (described in text). Second row (d-f): 850 hPa moisture flux vectors [qu, qv] and water vapor mixing ratio (shaded). Bottom row (g-i): 950 hPa Moisture flux convergence: MFC (described in text).

significantly weaker, -15.49 ms^{-1} and -7.83 ms^{-1}, respectively during the same time.

Fig. 13 shows the linear relationships during the tracked MCC between simulated maximum lower stratospheric water vapor above 4.2 ppmv and the following variables: maximum updrafts (500 and 100 hPa; Fig. 13a), maximum downdrafts (500 and 100 hPa; Fig. 13c), mean surface MFC (Fig. 13b), and lower troposphere water vapor (850 and 950 hPa; Fig. 13d). During the tracked MCC, the strongest linear correlation (R^2) is simulated between elevated maximum lower stratospheric water vapor and updrafts at 100 hPa (Fig. 13a) and downdrafts at 100 hPa (Fig. 13c). Additionally, lower tropospheric circulation, especially surface convergence (positive MFC; Fig. 13b) and maximum water vapor at 850 hPa (Fig. 13d), also have strong positive linear correlation with lower stratospheric water vapor. The transport of tropical moisture to the southern La Plata Basin via the SALLJ (e.g. Marengo et al., 2002, 2004; Montini et al., 2019) is likely an important source of water vapor contributing to elevated water vapor concentrations between 90 and 70 hPa. The influence of instability on UTLS thermodynamics is investigated next.

6. UTLS thermodynamics and lower stratosphere hydration

The following discussions investigate the relationships between tropopause levels and water vapor in the UTLS to better understand possible mechanisms related to the depth of overshooting and relationships with lower stratospheric hydration.

6.1. Double tropopause events

While double tropopauses (DT) are more frequent in tropical altitudes (Mehta et al., 2011), in this region (latitude range 22^0–37^0 S.), fair weather DT are generally more frequent near the subtropical jet stream

(Randel et al., 2007). They have been related to extra-tropical anticyclonic Rossby wave breaking associated with cold fronts connected to strong surface low pressure areas (Martius and Rivière, 2016) and related to mountain wave dynamics producing gravity waves (de laTorre et al., 2006). The interaction between large-scale mountain waves and the position of the upper-level jet stream (Fig. 3) may enhance the production of DT events (Peevey et al., 2012) in this region. However, this work examines DT events specifically related to deep convection, and the corresponding heights and concentrations of maximum water vapor in the lower stratosphere.

The tropopause can be identified in several different ways: chemical – e.g. abrupt changes in ozone concentrations, dynamical (e.g. potential vorticity), or thermal (e.g. changes in temperature lapse rates). Here we focus on identifying the thermal tropopause. Maddox and Mullendore (2018) compared several methods for tropopause identification during and after convection and found the best methods were the WMO thermal tropopause and static stability. Here, we use the WMO thermal tropopause definition. First, to calculate the temperature lapse rate, we linearly interpolated the original temperature profile in the UTLS (which varied between 100 and 400 m) to a constant 100 m vertical grid. Once interpolated, the temperature lapse rate was calculated ($-dT/dz$) from 5 to 20 km. Next, the primary tropopause was identified based on the WMO definition, which states that a thermal tropopause is located where the lapse rate decreases to less than or equal to 2 K/km (WMO, World Meteorological Organization, 1957). Following Peevey et al. (2012), the lapse rate was calculated above 5 km to avoid identifying low tropospheric inversions as the primary tropopause levels. Lastly, the location of the secondary tropopause was identified where the lapse rate increases above 3 °K/km within 2 km of the primary tropopause, and then decreases again to below 2 °K/km (modified from Peevey et al., 2012).

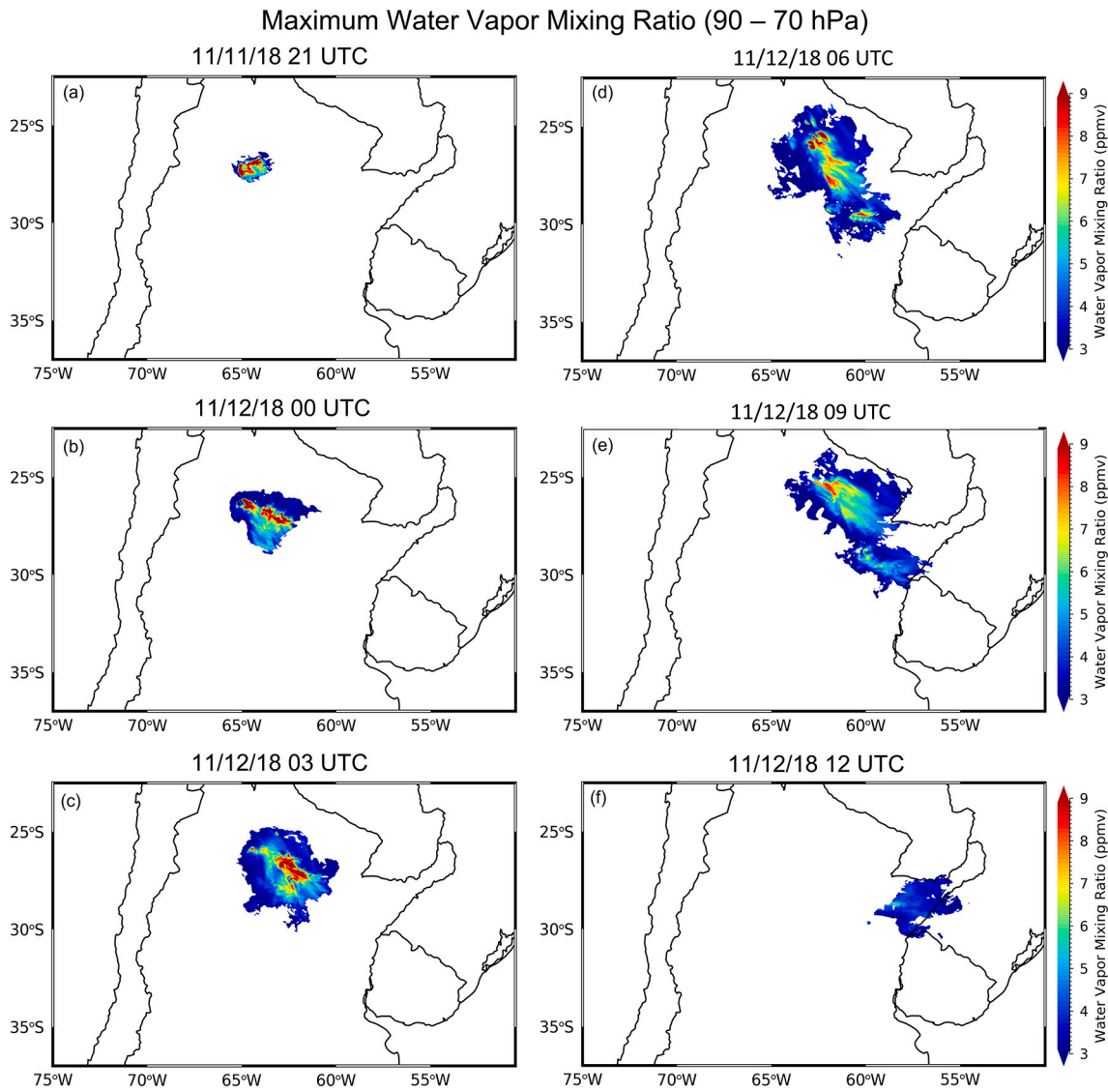We begin our DT analysis by identifying DT related to the tracked

Maximum Water Vapor Mixing Ratio (90 – 70 hPa)

Fig. 12. Clusters of deep convection between November 11, 21 UTC and November 12, 12 UTC (described in text). Maximum water vapor mixing ratios between 90 and 70 hPa.

Table 5
Properties associated with the MCC tracked during its lifetime.

|							
Track MCC clusters							
Time	21 UTC	00 UTC	03UTC	06 UTC	09 UTC	12UTC	15 UTC
Number of grid cells	2964	10,265	23,457	35,738	41,853	18,297	1114
Area (km²)	26,676	92,385	211,113	321,642	376,677	164,673	10,026
Maximum water vapor (ppmv)							
90–70 hPa	20.40	15.90	12.70	15.70	9.39	6.60	4.22
100 hPa	20.00	14.00	12.00	11.00	7.70	5.70	4.10
Lower stratosphere water vapor greater than or equal to 4.2 (ppmv)							
Number of grid points	1625	5292	10,257	12,386	13,326	2932	
Number of grid points with DT	919	1284	4693	6231	4621	2671	
Percentage of grid points with DT	57	24	46	50	35	91	
Maximum Updrafts (ms⁻¹)							
100 hPa	28.63	23.10	23.33	16.76	1.49	1.88	0.22
500 hPa	26.08	20.44	24.61	20.82	17.71	16.30	0.48
Maximum Downdrafts (ms⁻¹)							
100 hPa	−15.49	−10.36	−8.90	−4.95	−2.72	−1.85	−0.21
500 hPa	−7.83	−5.63	−7.16	−6.79	−7.31	−4.87	−0.13
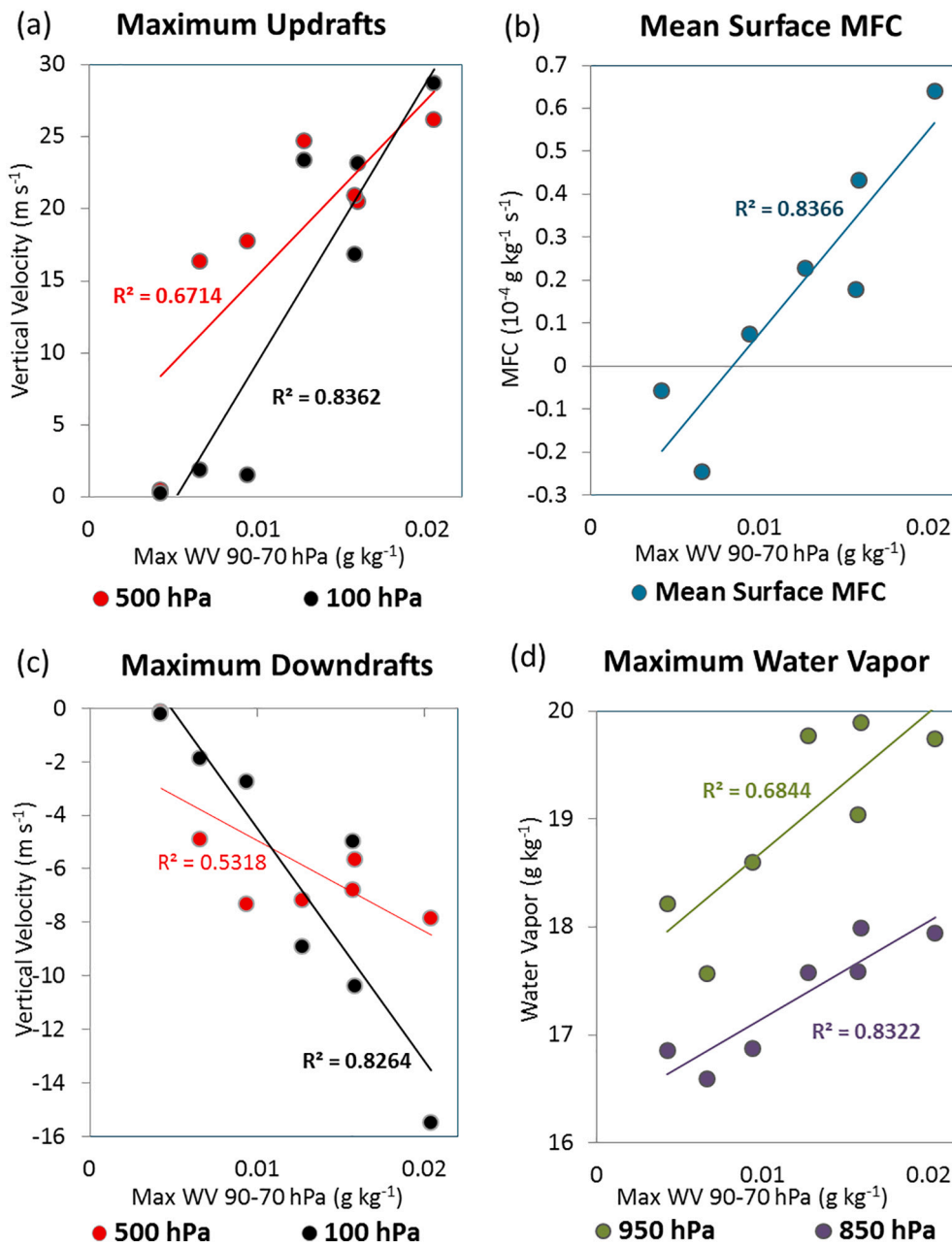
Fig. 13. For each tracked deep convective cluster. Maximum water vapor mixing ratio above 0.0042 g kg^{-1} between 90 and 70 hPa (x-axis) are compared to maximum updrafts (a), downdrafts (c), MFC (b) and maximum lower stratospheric water vapor (d).

MCC clusters (Table 5, lower half). Only grid points in the lower stratosphere (90–70 hPa) with maximum water vapor values above 4.2 ppmv were retained for this analysis. It should be noted that when this threshold was applied, the last time frame (November 23, 15 UTC) was removed from the MCC tracking (Table 5).

Based on the threshold, the cluster at 21 UTC had over 50% of the of grid points exceeding 4.2 ppmv associated with DT features (Table 5). At this time, this cluster showed the highest percentage of DT features (57%), the highest maximum water vapor mixing ratios in the lower stratosphere (20.40 ppmv), and the strongest updrafts and downdrafts at 500 and 100 hPa. The amount of water vapor progressively decreased until 03 UTC, accompanied by a decrease in the intensity of the updrafts. However, at 06 UTC the maximum water vapor increased to values comparable to 00 UTC between 90 and 70 hPa (15.70 ppmv), while maximum updrafts, although strong, continued to decrease (16.76 ms^{-1}). This enhancement in water vapor appeared related to an increase

in the fraction of DT (50%), suggesting that the presence of DT might have been the mechanism by which water vapor was further enhanced above 100 hPa, even with the decrease in the intensity of the updrafts. At 9:00 UTC, the magnitudes of the maximum updrafts are approximately 10% of what was simulated in the previous 3 h period, and the percentage of grid points associated with DT also decreased to 35%. With low support from both updrafts and DT, the maximum water vapor above 100 hPa is only 60% of what was observed 3 h earlier. At 12 UTC, as the system dissipated and updrafts weakened, the maximum water vapor values continued decreasing, and nearly 90% of all grid points exceeding 4.2 ppmv were associated with DT.

Fig. 14a, e and i show cross sections of lapse rates (shaded) during each type of deep convection: at 32.79°S for the DC, 26.04°S for the MCC, and 22.81°S for the squall line. The points for the primary and secondary thermal lapse rate tropopause levels are shown with filled dots. The latitudes for each cross section were chosen based on
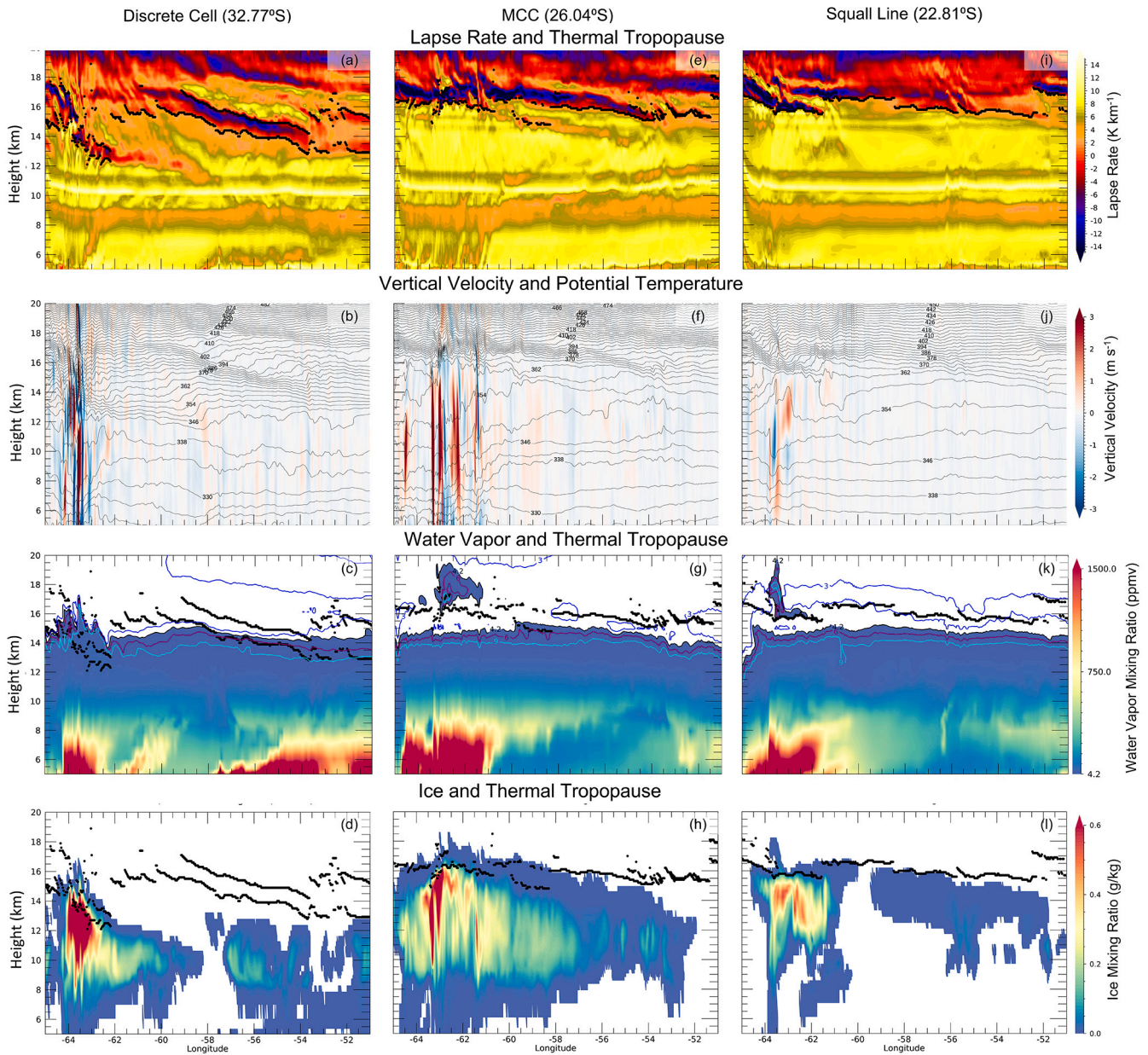
Fig. 14. Longitudinal cross sections (65–51°W) for each system: DC (a, b, c, and d), MCC (e, f, g, and h) and Squall line (i, j, k, and l).The temperature lapse rate ($-dT/dz$; shaded) and thermal tropopause levels (filled dots) are on the top panel (a, e and i) Vertical velocity (w; shaded) and potential temperature (theta; isotherms) are on the second panel (b, f and j). Water vapor mixing ratios greater than 4.2 ppmv (shaded; white areas are less than 4.2 ppmv), UTLS water vapor mixing ratio (line contours): 3 ppmv (blue), 4.2 ppmv (black), 6 ppmv (purple), 9 ppmv (cyan), and thermal tropopause levels (filled dots) are on the third panel (c, g and k). Ice mixing ratios (shaded) and thermal tropopause levels (filled dots) are on the fourth panel (d, h and l). (For interpretation of the references to colour in this figure legend, the reader is referred to the web version of this article.)

maximum water vapor concentrations in the lower stratosphere from 15 to 20 km during each convective event. The convective latent heat release during phase changes (condensation and freezing) appears to occur during each case of deep convection, which is indicated by the decrease in lapse rate in the mid and upper troposphere (Fig. 14a, e and i). Additionally, vertical velocity (shaded) and potential temperature (contour) (Figs. 14b, f and j) illustrate instability and enhanced updrafts, possibly in association with latent heat exchanges in the mid and upper troposphere (Tao and Li, 2016).

Water vapor mixing ratios during each convective type are shown based on the 4.2 ppmv threshold (Fig. 14 c, g, and k; shaded), with additional line contours in the UTLS (3, 4.2, 6, and 9 ppmv) to highlight regions of enhanced water vapor in the lower stratosphere. Areas in

Fig. 14c, g and k without shading (white) represent water vapor mixing ratios below the 4.2 ppmv threshold. In the MCC and Squall line categories (Fig. 14g and k respectively), a gap exists between water vapor at or near the thermal tropopause levels with higher water vapor concentrations aloft. This dry layer may assist in identifying hydration of the lower stratosphere and indicate irreversible mixing (Dauhut et al., 2018). One explanation for this result is ice crystal formation and latent heat release in the UTLS. Diabatic heating can produce positive net buoyancy and strong updrafts forcing ice aloft. At warmer levels in the lower stratosphere, ice is sublimated, producing higher water vapor concentrations (Dessler et al., 1995; Smith et al., 2017). This process appears to hydrate the lower stratosphere with the direct injection of ice particles (Khaykin et al., 2009). Fig. 14d, h and i show ice mixing ratios

that may support this explanation. Conversely, the DC event does not have a gap above the moist tropopause. While ice and water vapor are detected directly above the secondary tropopause, the lack of a dry layer and corresponding water vapor above indicates that the lower stratosphere is not hydrated at this location by discrete cell overshooting. Although ice crystal sublimation and detrainment typically occur on the scale of minutes, the 3-hourly output suggests that these processes may have contributed to the UTLS hydration.

For each convective category investigated here, water vapor detrainment in the lower stratosphere seems associated with a sharp change in lapse rate with height, coinciding with a sharp change in static stability ($\partial\theta/\partial z$). This is especially noted in the MCC and Squall line convective types (Fig. 14e, f, i, j). For both categories, large instability below the primary tropopause level is capped by a shallow stable layer (Fig. 14f and j; potential temperature contours), where steep potential temperature gradients are observed. This is indicative of previously described double tropopause events (Homeyer et al., 2014a). Below the sharp change in lapse rate, where temperature controls the formation of ice (Jensen et al., 2007), latent heat release during ice formation is likely responsible for instability and increased water vapor levels aloft due to updrafts.

6.2. UTLS mechanisms explaining maximum water vapor between 15 and 20 km

To further understand the mechanisms explaining the height of maximum water vapor levels, individual grid points with large maximum water vapor concentrations in the lower stratosphere are examined during each type of deep convection. Here we show profiles of water vapor mixing ratio, ice mixing ratio, air temperature (Fig. 15), and profiles of lapse rates and vertical velocity (Fig. 16) during each category of deep convection. The grid point at 63.78°W, 32.79°S is related to the DC. The background levels were only observed above 17 km (not shown). At this grid point, large ice mixing ratios were observed from 13.4–15.3 km and collocated with elevated water vapor mixing ratios. Generally, the ice and water vapor mixing ratios decrease with height. However, just above 13 km, ice increased as water vapor decreased, and net vertical movement was strongly positive (Fig. 16; Discrete Cells right panel). Despite this hydrated mixed layer in the UTLS and updrafts below the primary tropopause, no significant decrease in the water vapor was detected with a hydrating layer above. Additionally, vertical velocity was negative above the secondary tropopause. Warm tropopause temperatures and strong downdrafts above the secondary tropopause may also explain the lack of stratosphere hydration over this location compared to the MCC and Squall line events.

The grid point at 62.91°W, 26.03°S was related to the MCC and background water vapor values are found in two layers: approximately 15–16.5 km and just below 20 km (Fig. 15, MCC left panel). During the MCC, elevated ice mixing ratio values were observed below the primary thermal tropopause level (16.3 km) and coincided with the dry water vapor layers (background levels). Additionally, a sharp change in lapse rate began at approximately 16.5 km and a secondary tropopause was identified at 17 km. At this altitude maximum water vapor levels sharply increased, and vertical velocity shifted from negative to positive values at 17.5 km, where strong updrafts forced water vapor aloft (Fig. 16, MCC right panel). This grid point indicates a dry layer in tropopause water vapor with a hydrated layer above, as observed in the longitude-height profiles (Fig. 14). This point indicates lower stratospheric hydration.

Lastly, the grid point at 63.50°W, 22.81°S was related to the Squall line and background values were found in multiple dry layers above 13 km: approximately 15 km, 17.2 km and 20 km (Fig. 15 Squall Line left panel). At this grid point, a deep double tropopause event occurred, and the thermal (lapse rate) tropopauses were identified at 15.7 km and 16.3 km. Elevated ice mixing ratios occurred from 13 to 16 km, and the maximum levels of ice were found at 15 km and coincided with a dry water vapor layer. Between the two tropopause layers (approximately

15.8 and 17.4 km), water vapor concentrations above 5 ppmv were observed up to 17 km, and small concentrations of ice were observed between 17.1 and 17.7 km. Additionally, the lapse rates at this grid point were subject to two sharp changes, and at 17 km the increased ice mixing ratios were detected where the second lapse rate minima indicated rapid cooling. Above this level, maximum water vapor (greater than 10 ppmv) was observed at 17.9 km and a secondary maximum was observed at 19.1 km. At 20 km, water vapor concentrations began to return to background levels. Like the MCC example, this grid point also shows a dry layer in tropopause water vapor with a hydrated layer above, as observed in the earlier longitude-height profiles (Fig. 14). This point also indicates lower stratospheric hydration.

7. Conclusions

The main goal of this study was to investigate mechanisms related to deep convection capable of perturbing the tropopause boundary, contributing to troposphere-to-stratosphere exchanges over the La Plata Basin using WRF simulations. Additionally, this study evaluated mechanisms driving convective overshooting and the height of maximum water vapor with focus on the La Plata Basin. Deep convection was evaluated during three types of convective systems during the RELAM-PAGO field campaign: discrete cells (DC), Mesoscale Convective Complex (MCC) and cold front boundary (Squall line). Three sensitivity tests were performed to investigate the importance of vertical resolution in the boundary layer and UTLS in reproducing observed double tropopause features. These experiments indicated that the best configuration was the 3 km horizontal grid spacing with 75 user assigned η levels concentrated in the boundary layer and UTLS, avoiding abrupt changes in height between eta levels. With this configuration, WRF simulated the location and extent of the mature MCC reasonably well and showed an improvement in RMSE temperature and wind speed compared to the other two runs. More importantly, the temperature profiles showed an improvement in detecting double tropopause features.

We evaluated the influence of tropospheric flow on the development of deep convection and its contribution to maximum lower stratospheric water vapor concentrations. We found that weak meridional moisture transport occurred during the DC, while strong meridional and moisture transport occurred during the MCC and Squall line associated with the presence and intensity of the SALLJ. For the MCC, we observed a strong linear correlation between maximum UTLS water vapor and updrafts and downdrafts at 100 hPa. However, the meridional moisture transport at 850 hPa and mean MFC at 950 hPa also exhibited strong correlation with the maximum UTLS water vapor during the MCC. From a thermodynamic perspective, instability in the UTLS and convective induced DT appeared to contribute to the increase in water vapor levels in the lower stratosphere.

WRF detected double tropopause events for each convective system examined here, and they were collocated with enhanced maximum water vapor levels in the lower stratosphere. A key result of this study is that the primary source of lower stratospheric hydration appears related to ice near the thermal tropopause. Cold primary tropopause temperatures and the presence of moisture seem to contribute to ice formation in the UTLS leading to instability via latent heat exchanges and strong updrafts. During these events, a sharp change in lapse rate occurs where rapid cooling with height is followed by rapid warming. A possible mechanism explaining this is the detrainment of ice in the lower stratosphere and subsequent sublimation, which would contribute to elevated water vapor mixing ratios and localized downdrafts.

Additionally, not all convective systems investigated here hydrated the stratosphere. While all systems have hydrated layers between the primary and secondary tropopause levels, only the MCC and Squall line hydrated the lower stratosphere. Among the three categories, DC had the warmest primary tropopause temperatures (~200 K) and weakest updrafts at 100 hPa. Additionally, the primary tropopause was located at lower altitudes (~14 km) compared to the MCC and Squall line. During
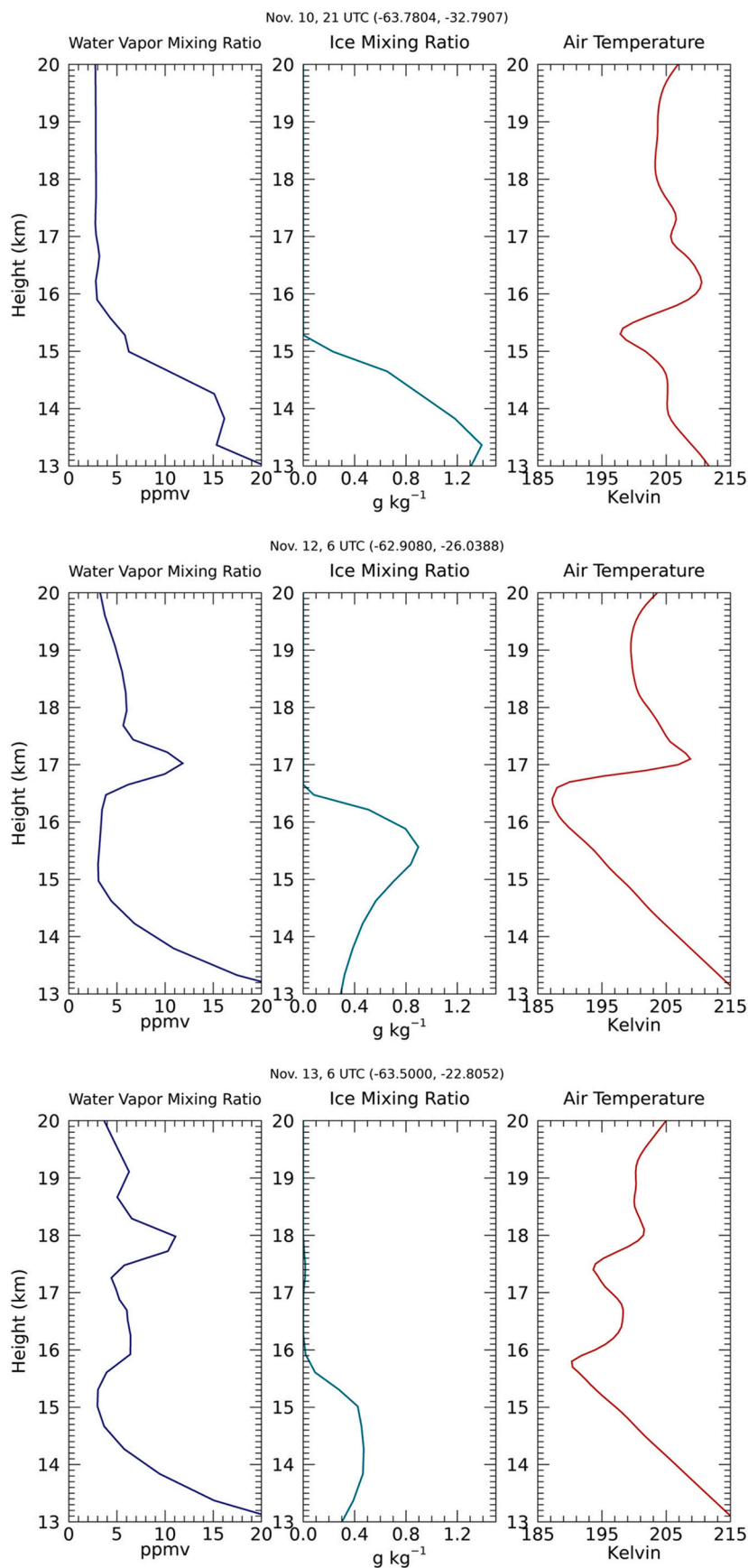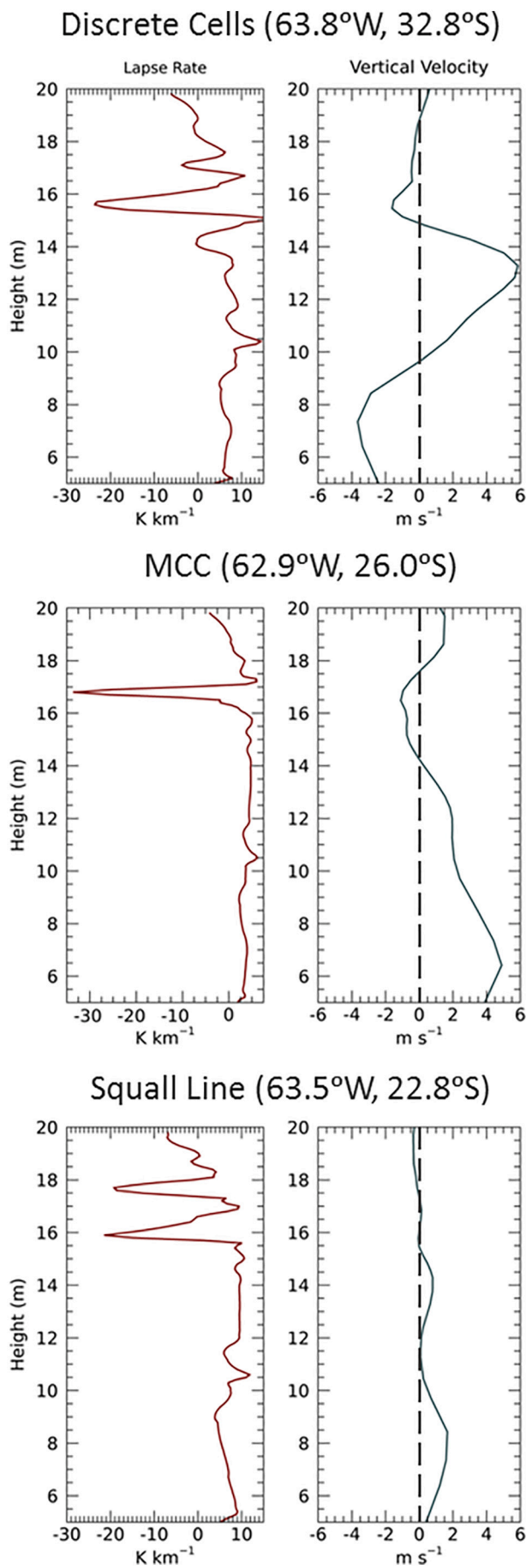
Fig. 15. Upper troposphere – lower stratosphere profiles (13–20 km) of WRF data: water vapor mixing ratio (left column), ice mixing ratio (center column), air temperature (right column). Grid points are selected for each convective type: discrete cells (top panel), MCC (center panel) and Squall line (bottom panel).

Fig. 16. Profiles (6–20 km) of WRF data: temperature lapse rate (left column) and vertical velocity (right column). Grid points are selected for each convective type: discrete cells (top panel), MCC (center panel) and Squall line (bottom panel).

DC, the tropopause was hydrated where a mixed layer of water vapor and ice was located above the primary tropopause and extended just above the secondary tropopause. However, directly above the primary tropopause, temperatures warmed quickly and strong updrafts were not observed. During this event, deep convective overshooting did not appear to hydrate the lower stratosphere. No pocket of air with water vapor mixing ratios above background levels were observed above the overshooting. While the mixing of ice and water vapor likely contributed to the large instability between tropopause layers, net vertical velocity was negative above the secondary tropopause, which would explain why water vapor was not observed above 17 km.

The MCC and Squall line categories exhibited colder primary tropopause temperatures (187–191 K), higher primary tropopause heights (~16 and ~ 15.75 km, respectively), and pockets of low water vapor concentrations in and above the tropopause. Lower stratospheric hydration was observed in both convective types to nearly 20 km. Additionally, above 15 km the water vapor and ice concentrations were stratified, and the presence of ice and water vapor mixing ratios were in layers rather than mixed, as observed with the DC system. This may have contributed to the enhanced instability below the primary tropopause level and the strong positive vertical velocity capable of overshooting tropospheric material beyond the secondary tropopause. This mechanism can explain the heights of maximum water vapor observed hydrating the lower stratosphere.

While this study relies entirely on regional modeling results, the mechanisms proposed here to explain the presence of enhanced water vapor mixing ratios in the UTLS associated with deep convective systems over the La Plata Basin are consistent with previous observational studies over the U.S (e.g., Smith et al., 2017; Corti et al., 2008). More importantly, these mechanisms are relevant for radiation budgets and stratospheric chemistry and could affect ozone concentration with implications for people and the environment (Smith, 2021). The extent of the contribution of water vapor on stratospheric chemistry and ozone destruction in the LPB would require further investigation.

Author statement

Brandi Gamelin: Conceptualization, methodology, data processing and analyses, and manuscript draft and revisions. Leila Carvalho: Supervision, methodology and manuscript editing and revisions. Charles Jones: Data management and manuscript revisions.

Declaration of Competing Interest

The authors declare that they have no known competing financial interests or personal relationships that could have appeared to influence the work reported in this paper.

Acknowledgments

(caption on next column)

References

Baisya, H., Pattnaik, S., 2019. Orographic effect and multiscale interactions during an extreme rainfall event. Environ. Res. Commun. 1, 051002.

Banacos, P.C., Schultz, D.M., 2005. The use of moisture flux convergence in forecasting convective initiation: historical and operational perspectives. Wea. Forecast. 20, 351–366. https://doi.org/10.1175/WAF858.1.

Bates, D.R., Nicolet, M., 1950. The photochemistry of atmospheric water vapor. J. Geophys. Res. 55, 301–327.

Berbery, E.H., Collini, E.A., 2000. Springtime precipitation and water vapor flux over southeastern South America. Mon. Weather Rev. 128, 1328–1346. https://doi.org/10.1175/1520-0493(2000)128<1328:SPAWVF>2.0.CO;2.

Bigelbach, B.C., Mullendore, G.L., Starzec, M., 2014. Differences in deep convective transport characteristics between quasi-isolated strong convection and mesoscale convective systems using seasonal WRF simulations. J. Geophys. Res. Atmos. 119, 11,445–11,455. https://doi.org/10.1002/2014JD021875.

Brasseur, G., Solomon, S., 2005. Composition and chemistry. In: Aeronomy of the Middle Atmosphere, 3rd edn. Springer, Dordrecht, Netherlands, pp. 265–422.

Brewer, A.W., 1949. Evidence for a world circulation provided by the measurements of helium and water vapor distribution in the stratosphere. Q. J. Roy. Meteor. Soc. 75, 351–363.

Brooks, H.E., Lee, J.W., Craven, J.P., 2003. The spatial distribution of severe thunderstorm and tornado environments from global reanalysis data. Atmos. Res. 67, 73–94.

Carvalho, L.M.V., Jones, C., 2001. A satellite method to identify structural properties of mesoscale convective systems based on maximum spatial correlation tracking technique (MASCOTTE). J. Appl. Meteorol. 40, 1683–1701.

Corti, T., Luo, B.P., De Reus, M., Brunner, D., Cairo, F., Mahoney, M.J., Martucci, G., Matthey, R., Mitev, V., Dos Santos, F.H., Schiller, C., 2008. Unprecedented evidence for deep convection hydrating the tropical stratosphere. Geophys. Res. Lett. 35 (10).

Dauhut, T., Chaboureau, J., Haynes, P.H., Lane, T.P., 2018. The mechanisms leading to a stratospheric hydration by overshooting convection. J. Atmos. Sci. 75, 4383–4398. https://doi.org/10.1175/JAS-D-18-0176.1.

de laTorre, A., Alexander, P., Llamedo, P., Menéndez, C., Schmidt, T., Wickert, J., 2006. Gravity waves above the Andes detected from GPS radio occultation temperature profiles: Jet mechanism? Geophys. Res. Lett. 33, L24810. https://doi.org/10.1029/2006GL027343.

Dee, D.P., Uppala, S.M., Simmons, A.J., Berrisford, P., Poli, P., Kobayashi, S., Andrae, U., Balmaseda, M.A., Balsamo, G., Bauer, P., Bechtold, P., Beljaars, A.C.M., van de Berg, L., Bidlot, J., Bormann, N., Delsol, C., Dragani, R., Fuentes, M., Geer, A.J., Haimberger, L., Healy, S.B., Hersbach, H., Holm, E.V., Isaksen, L., Kallberg, P., Köhler, M., Matricardi, M., McNally, A.P., Monge-Sanz, B.M., Morcette, J.-J., Park, B.-K., Peubey, C., de Rosnay, P., Tavolato, C., Thepaut, J.-N., Vitart, F., 2011. The ERA-Interim reanalysis: Configuration and performance of the data assimilation system. Q. J. Roy. Meteor. Soc. 137, 553–597. https://doi.org/10.1002/qj.828.

Dessler, A.E., Hintsa, E.J., Weinstock, E.M., Anderson, J.G., Chan, K.R., 1995. Mechanisms controlling water vapor in the lower stratosphere: "a tale of two stratospheres". J. Geophys. Res. 100 (D11), 23, 167–23,172.

Dessler, A.E., Sherwood, S.C., 2004. Effect of convection on the summertime extratropical lower stratosphere. J. Geophys. Res. 109, D23301. https://doi.org/10.1029/2004JD005209.

Ferreira, R.N., Rickenbach, T.M., Herdies, D.L., Carvalho, L.M.V., 2003. Variability of South American convective cloud systems and tropospheric circulation during January–March 1998 and 1999. Mon. Weather Rev. 131 (5), 961–973.

Forster, P.M.F., Shine, K.P., 2002. Assessing the climate impact of trends in stratospheric water vapor. Geophys. Res. Lett. 29 (6), 10. https://doi.org/10.1029/2001GL013909.

Giangrande, S.E., Collis, S., Straka, J., Protat, A., Williams, C., Krueger, S., 2013. A summary of convective-core vertical velocity properties using ARM UHF wind profilers in Oklahoma. J. Appl. Meteorol. Climatol. 52 (10), 2278–2295. Retrieved Sep 2, 2021. https://journals.ametsoc.org/view/journals/apme/52/10/jamc-d-12-0185.1.xml.

Grell, G.A., Devenyi, D., 2002. A generalized approach to parameterizing convection combining ensemble and data assimilation techniques. Geophys. Res. Lett. 29, 1693.

Grell, G.A., Freitas, S.R., 2014. Scale and aerosol aware stochastic convective parameterization for weather and air quality modeling. Atmos. Chem. Phys. 14, 5233–5250. https://doi.org/10.5194/acp-14-5233-2014.

Gutzler, D.S., Wood, T.M., 1990. Structure of large-scale convective anomalies over Tropical Oceans. J. Clim. 3, 483–496.

Hemanth, et al., 2018. Cross tropopause flux observed at sub-daily scales over the south Indian monsoon regions. Atmos. Res. 201 https://doi.org/10.1016/j.atmosres.2017.10.017.

Heymsfield, G.M., Tian, L., Heymsfield, A.J., Li, L., Guimond, S., 2010. Characteristics of deep tropical and subtropical convection from nadir-viewing high-altitude airborne Doppler radar. J. Atmos. Sci. 67 (2), 285–308. Retrieved Sep 2, 2021. https://journals.ametsoc.org/view/journals/atsc/67/2/2009jas3132.1.xml.

Higgins, R.W., Yao, Y., Yarosh, E.S., Janowiak, J.E., Mo, K.C., 1997. Influence of the Great Plains low-level jet on summertime precipitation and moisture transport over the Central United States. J. Clim. 10 (3), 481–507.

Holton, J.R., Haynes, P.H., McIntyre, M.E., Douglass, A.R., Rood, R.B., Pfister, L., 1995. Stratosphere-troposphere exchange. Rev. Geophys. 33, 403–440.

Homeyer, C.R., 2015. Numerical simulations of extratropical tropopause-penetrating convection: Sensitivities to grid resolution. J. Geophys. Res. Atmos. 120, 7174–7188. https://doi.org/10.1002/2015JD023356.

Homeyer, C.R., Pan, L.L., Barth, M.C., 2014a. Transport from convective overshooting of the extratropical tropopause and the role of large-scale lower stratosphere stability. J. Geophys. Res. Atmos. 119, 2220–2240. https://doi.org/10.1002/2013JD020931.

Homeyer, C.R., et al., 2014b. Convective transport of water vapor into the lower stratosphere observed during double tropopause events. J. Geophys. Res. Atmos. 119, 10941–10958. https://doi.org/10.1002/2014JD021485.

Homeyer, C., McAuliffe, J.D., Bedka, K.M., 2017. On the development of above-anvil cirrus plumes in extratropical convection. J. Atmos. Sci. 74, 1617–1633.

Hong, S.-Y., Noh, Y., Dudhia, J., 2006. A new vertical diffusion package with an explicit treatment of entrainment processes. Mon. Weather Rev. 134, 2318–2341. https://doi.org/10.1175/MWR3199.1.

Hurst, D.F., Oltmans, S.J., Vömel, H., Rosenlof, K.H., Davis, S.M., Ray, E.A., Hall, E.G., Jordan, A.F., 2011. Stratospheric water vapor trends over Boulder, Colorado: Analysis of the 30 year Boulder record. J. Geophys. Res. 116, D02306. https://doi.org/10.1029/2010JD015065.

Iacono, M.J., Delamere, J.S., Mlawer, E.J., Shephard, M.W., Clough, S.A., Collins, W.D., 2008. Radiative forcing by long–lived greenhouse gases: calculations with the AER radiative transfer models. J. Geophys. Res. 113, D13103.

Janjic, Z.I., 1994. The Step–Mountain Eta coordinate model: further developments of the convection, viscous sublayer, and turbulence closure schemes. Mon. Weather Rev. 122, 927–945.

Jensen, E., Ackerman, A.S., Smith, J.A., 2007. Can overshooting convection dehydrate the tropical tropopause layer? J. Geophys. Res. 112, D11209. https://doi.org/10.1029/2006JD007943.

Jones, C., 2019. Recent changes in the South America low-level jet. NPJ Clim. Atmos. Sci. 2, 20. https://doi.org/10.1038/s41612-019-0077-5.

Kain, J.S., 2004. The Kain–Fritsch convective parameterization: an update. J. Appl. Meteorol. 43, 170–181.

Khaykin, S., Pommereau, J.-P., Korshunov, L., Yushkov, V., Nielsen, J., Larsen, N., Christensen, T., Garnier, A., Lukyanov, A., Williams, E., 2009. Hydration of the lower stratosphere by ice crystal geysers over land convective systems. Atmos. Chem. Phys. 8 https://doi.org/10.5194/acpd-8-15463-2008.

Laing, A.G., Fritsch, J.M., 1997. The global population of mesoscale convective complexes. Q. J. R. Meteorol. Soc. 123 (538), 389–405.

Lambert, A., Read, W., Livesey, N., 2020. MLS/Aura Level 2 Water Vapor (H2O) Mixing Ratio V005, Greenbelt, MD, USA. Goddard Earth Sciences Data and Information Services Center (GES DISC). https://doi.org/10.5067/Aura/MLS/DATA2508.

Le, T.V., Gallus Jr., W.A., 2012. Effect of an extratropical mesoscale convective system on water vapor transport in the upper troposphere/lower stratosphere: a modeling study. J. Geophys. Res. 117, D03111. https://doi.org/10.1029/2011JD016685.

Le Texier, H., Solomon, S., Garcia, R.R., 1988. The role of molecular hydrogen and methane oxidation in the water vapour budget of the stratosphere. Q. J. R. Meteorol. Soc. 114, 281–295. https://doi.org/10.1002/qj.49711448002.

Liu, N., Liu, C., 2016. Global distribution of deep convection reaching tropopause in 1 year GPM observations. J. Geophys. Res. Atmos. 121, 3824–3842. https://doi.org/10.1002/2015JD024430.

Maddox, E.M., Mullendore, G.L., 2018. Determination of best tropopause definition for convective transport studies. J. Atmos. Sci. 75 (10), 3433–3446. Retrieved Sep 14, 2021, from. https://journals.ametsoc.org/view/journals/atsc/75/10/jas-d-18-0032.1.xml.

Marengo, J.A., Douglas, M.W., Dias, P.L.S., 2002. The South American low-level jet east of the Andes during the 1999 LBA-TRMM and LBA-WET AMC campaign. J. Geophys. Res. 107 (D20), 8079. https://doi.org/10.1029/2001JD001188.

Marengo, J.A., Soares, W.R., Saulo, C., Nicolini, M., 2004. Climatology of the low-level jet east of the Andes as derived from the NCEPNCAR reanalyses: characteristics and temporal variability. J. Clim. 17 (12), 2261–2280. https://doi.org/10.1175/15200442(2004)017<2261:COTLJE>2.0.CO;2.

Martius, O., Rivière, G., 2016. Rossby wave breaking: climatology, interaction with low-frequency climate variability, and links to extreme weather events. In: Li, J., Swinbank, R., Grotjahn, R., Volkert, H. (Eds.), Dynamics and Predictability of Large-Scale, High-Impact Weather and Climate Events (Special Publications of the International Union of Geodesy and Geophysics). Cambridge University Press, Cambridge, pp. 69–78. https://doi.org/10.1017/CBO9781107775541.006.

Massie, S., Gettelman, A., Randel, W., Baumgardner, D., 2002. Distribution of tropical cirrus in relation to convection. J. Geophys. Res. 107 (D21), 4591. https://doi.org/10.1029/2001JD001293.

Mehta, et al., 2011. Multiple tropopauses in the tropics: a cold point approach. J. Geophys. Res. 116, D20105. https://doi.org/10.1029/2011JD016637.

Montini, T.L., Jones, C., Carvalho, L.M.V., 2019. The South American low-level jet: a new climatology, variability, and changes. J. Geophys. Res.-Atmos. 124, 1200–1218. https://doi.org/10.1029/2018JD029634.

Morrison, H., Thompson, G., Tatarskii, V., 2009. Impact of cloud microphysics on the development of trailing stratiform precipitation in a simulated squall line: comparison of one– and two–moment schemes. Mon. Weather Rev. 137, 991–1007. https://doi.org/10.1175/2008MWR2556.1.

Mulholland, J.P., Nesbitt, S.W., Trapp, R.J., Rasmussen, K.L., Salio, P.V., 2018. Convective storm life cycle and environments near the Sierras de Córdoba, Argentina. Mon. Weather Rev. 146, 2541–2557. https://doi.org/10.1175/MWR-D-18-0081.1.

Mullendore, G.L., Durran, D.R., Holton, J.R., 2005. Cross-tropopause tracer transport in midlatitude convection. J. Geophys. Res. 110, D06113. https://doi.org/10.1029/2004JD005059.

Nesbitt, S.W., Salio, P.V., Ávila, E., Bitzer, P., Carey, L., Chandrasekar, V., Deierling, W., Dominguez, F., Dillon, M.E., Garcia, C.M., Gochis, D., 2021. A storm safari in subtropical South America: Proyecto RELAMPAGO. Bull. Am. Meteorol. Soc. 102 (8), E1621–E1644.

Niu, G.-Y., Yang, Z.-L., Mitchell, K.E., Chen, F., Ek, M.B., Barlage, M., Kumar, A., Manning Niyogi, D., Rosero, E., Tewari, M., Xia, Y., 2011. The community Noah land surface model with multiparameterization options (Noah–MP): 1. Model description and evaluation with local–scale measurements. J. Geophys. Res. 116, D12109.

Pan, L.L., Randel, W.J., Gary, B.L., Mahoney, M.J., Hintsa, E.J., 2004. Definitions and sharpness of the extratropical tropopause: a trace gas perspective. J. Geophys. Res. 109, D23103. https://doi.org/10.1029/2004JD004982.

Paulson, C.A., 1970. The mathematical representation of wind speed and temperature profiles in the unstable atmospheric surface layer. J. Appl. Meteorol. 9, 857–861.

Peevey, T.R., Gille, J.C., Randall, C.E., Kunz, A., 2012. Investigation of double tropopause spatial and temporal global variability utilizing High Resolution Dynamics Limb Sounder temperature observations. J. Geophys. Res. 117, D01105. https://doi.org/10.1029/2011JD016443.

Phoenix, D.B., Homeyer, C.R., 2021. Simulated Impacts of tropopause-overshooting convection on the chemical composition of the upper troposphere and lower stratosphere. J. Geophys. Res.-Atmos. 126, e2021JD034568 https://doi.org/10.1029/2021JD034568.

Randel, W., Jensen, E.J., 2013. Physical processes in the tropical tropopause layer and their roles in a changing climate Nat. Geosci. 6, 169–176.

Randel, W.J., Seidel, D.J., Pan, L.L., 2007. Observational characteristics of double tropopauses. J. Geophys. Res. 112, D07309. https://doi.org/10.1029/2006JD007904.

Rasmussen, K.L., Houze, R.A., 2016. Convective initiation near the andes in subtropical South America. Mon. Weather Rev. 144, 2351–2374. https://doi.org/10.1175/MWR-D-15-0058.1.

Rasmussen, K.L., Houze Jr., R.A., 2011. Orogenic convection in subtropical South America as seen by the TRMM satellite. Mon. Weather Rev. 139, 2399–2420.

Ratnam, et al., 2016. Effect of tropical cyclones on the stratosphere-troposphere exchange observed using satellite observations over North Indian Ocean. Atmosph. Chem. Phys. Discus. 1–30.

Read, W.G., et al., 2007. Aura Microwave Limb Sounder upper tropospheric and lower stratospheric H_2O and relative humidity with respect to ice validation. J. Geophys. Res. 112, D24S35. https://doi.org/10.1029/2007JD008752.

Robinson, F.J., Sherwood, S.C., 2005. Modeling the impact of entrainment on the tropical tropopause. AMS 63, 1013–1027.

Romatschke, U., Houze Jr., R.A., 2010. Extreme summer convection in South America. J. Clim. 23, 3761–3791.

Ruiz, J.J., Saulo, C., Nogués-Paegle, J., 2010. WRF Model Sensitivity to choice of parameterization over South America: validation against surface variables. Mon. Weather Rev. 138, 3342–3355. https://doi.org/10.1175/2010MWR3358.1.

Salio, P., Nicolini, M., Saulo, A.C., 2002. Chaco low-level jet events characterization during the austral summer-season. J. Geophys. Res. 107 (D24), 4816–4832.

Salio, P., Nicolini, M., Zipser, E.J., 2007. Mesoscale convective systems over Southeastern South America and their relationship with the South American low-level jet. Mon. Weather Rev. 135, 1290–1309. https://doi.org/10.1175/MWR3305.1.

Seinfeld, J.H., Pandis, S.N., 1998. Atmospheric Chemistry and Physics: From Air Pollution to Climate Change. John Wiley & Sons, Inc., New York, NY, p. 1360.

Simmons, A., Uppala, S., Dee, D., Kobayashi, S., 2006. ERA-Interim: new ECMWF reanalysis products from 1989 onwards. ECMWF Newslett. 110, 26–35.

Skamarock, W.C., Klemp, J.B., Dudhia, J., Gill, D.O., Barker, D.M., Duda, M.G., Huang, X.-Y., Wang, W., Powers, J.G., 2008. A Description of the Advanced Research WRF Version 3. NCAR Technical Note NCAR/TN-475+STR. https://doi.org/10.5065/D68S4MVH.

Smith, J.B., 2021. Convective hydration of the stratosphere. Science 373 (6560), 1194–1195.

Smith, J.B., Wilmouth, D.M., Bedka, K.M., Bowman, K.P., Homeyer, C.R., Dykema, J.A., Sargent, M.R., Clapp, C.E., Leroy, S.S., Sayres, D.S., Dean-Day, J.M., 2017. A case study of convectively sourced water vapor observed in the overworld stratosphere over the United States. J. Geophys. Res.-Atmos. 122 (17), 9529–9554.

Stenke, A., Grewe, V., 2005. Simulation of stratospheric water vapor trends: impact on stratospheric ozone chemistry. Atmos. Chem. Phys. 5, 1257–1272. https://doi.org/10.5194/acp-5-1257-2005.

Tao, W.-K., Li, X., 2016. The relationship between latent heating, vertical velocity, and precipitation processes: the impact of aerosols on precipitation in organized deep convective systems. J. Geophys. Res. Atmos. 121, 6299–6320. https://doi.org/10.1002/2015JD024267.

Tiedtke, M., 1989. A comprehensive mass flux scheme for cumulus parameterization in large–scale models. Mon. Weather Rev. 117, 1779–1800.

Trapp, R.J., Coauthors, 2020. Multiple-platform and multiple-doppler radar observations of a supercell thunderstorm in South America during RELAMPAGO. Mon. Weather Rev. 148, 3225–3241. https://doi.org/10.1175/MWR-D-20-0125.1.

Vera, C., Baez, J., Douglas, M., Emmanuel, C.B., Marengo, J., Meitin, J., Nicolini, M., Nogues-Paegle, J., Paegle, J., Penalba, O., Salio, P., Saulo, C., Silva Dias, M.A., Dias, P.S., Zipser, E., 2006. The South American low-level jet experiment. Bull. Amer. Meteor. Soc. 87, 63–77. https://doi.org/10.1175/BAMS-87-1-63.

Vernekar, A.D., Kirtman, B.P., Fennessy, M.J., 2003. Low-level jets and their effects on the South American Summer climate as simulated by the NCEP Eta Model. J. Clim. 16, 297–311. https://doi.org/10.1175/1520-0442(2003)016<0297:LLJATE>2.0.CO;2.

Wang, P.K., 2003. Moisture plumes above thunderstorm anvils and their contributions to cross-tropopause transport of water vapor in midlatitudes. J. Geophys. Res. 108, D002581. https://doi.org/10.1029/2002JD002581.

WMO, World Meteorological Organization, 1957. Meteorology — a three dimensional science: second session of the Commission for Aerology. WMO Bull. IV (4), 134–138.

Zhang, C., Wang, Y., Hamilton, K., 2011. Improved representation of boundary layer clouds over the southeast pacific in ARW–WRF using a modified Tiedtke cumulus parameterization scheme. Mon. Weather Rev. 139, 3489–3513.

Zipser, E.J., Cecil, D.J., Liu, C., Nesbitt, S.W., Yorty, D.P., 2006. Where are the most intense thunderstorms on earth? Bull. Amer. Meteor. Soc. 87, 1057–1072. https://doi.org/10.1175/BAMS-87-8-1057.